

STRUCTURE EFFECTS
IN HEAVY-ION TRANSFER
REACTION TO THE CONTINUUM

by

DARYUSH ILA
BACHELOR OF SCIENCE
TEHRAN UNIVERSITY, IRAN (1978)

SUBMITTED TO THE DEPARTMENT OF
PHYSICS IN PARTIAL
FULFILLMENT OF THE
REQUIREMENTS FOR THE
DEGREE OF
MASTER OF SCIENCE IN
PHYSICS

at the

MASSACHUSETTS INSTITUTE OF TECHNOLOGY


January, 1982

© Massachusetts Institute of Technology 1982

Signature of Author


Department of Physics Jan. 8, 1982

Certified by


Stephen G. Steadman
Thesis Supervisor

Accepted by


George F. Koster
Chairman, Department Committee

Archives
MASSACHUSETTS INSTITUTE
OF TECHNOLOGY

APR 08 1982

LIBRARIES

STRUCTURE EFFECTS IN HEAVY-ION
TRANSFER REACTIONS TO THE CONTINUUM

by

DARYUSH ILA

SUBMITTED TO THE DEPARTMENT OF PHYSICS
IN PARTIAL FULFILMENT OF THE REQUIREMENTS
FOR THE DEGREE OF MASTER OF SCIENCE
IN PHYSICS

ABSTRACT

Heavy-ion transfer reactions to highly excited states are studied in a constrained phase-space approach. Measurements are made of energy spectra for different exit channels by bombarding 98 MeV ^{16}O ions on targets with masses near closed shell nuclei ($^{205}_{81}\text{Tl}$ and $^{197}_{79}\text{Au}$) at about the grazing scattering angle of 70 degrees.

The charge identification of the projectile-like particles is obtained from the specific energy loss $dE/dX \sim MZ^2/E$ using a combination of a silicon surface barrier detector and a proportional wire chamber as ΔE . There is also a carbon foil time-pick-off between the target and the detector such that the time-of-flight, which is proportional to $\sqrt{M/E_T}$, could be used to separate the masses of isotopes for a given Z .

These excitation spectra were used to study the dependence of the energy-integrated differential cross-section, which is proportional to the branching ratio, and the effective optimal Q -value to the number of steps in the transfer reaction. The results have been examined in terms of a phenomenological constrained phase-space approach.

The results of the effective optimal Q -value and energy-integrated differential cross-section show that there is a structure effect in the ^{15}N exit channel in the $^{16}\text{O} + ^{205}\text{Tl}$ reaction. The heavy ejectile of this reaction is $^{206}_{82}\text{Pb}$.

Thesis supervisor: Stephen Steadman

Title: Associate Professor of Physics.

TABLE OF CONTENTS:

Acknowledgments	5
Figure Captions.....	6
List of Tables.....	9
References.....	10
CHAPTER I: Introduction to Heavy Ion Reactions.....	12
I-A. Background.....	12
I-B. Scattering of Heavy Ions as	
Semi-classical Objects.....	21
CHAPTER II: Surprisal Analysis.....	28
II-A. One-Constraint Analysis.....	30
II-B. Two-Constraint Analysis.....	31
CHAPTER III: Experimental Method... ..	37
CHAPTER IV: Data Analysis and Results.....	48
CHAPTER V: Summary and Conclusions.....	71

ACKNOWLEDGEMENTS:

Professor Stephen Steadman has suggested and supervised the work presented in this thesis. I gratefully acknowledge his patience, and support.

I also appreciate the help of the Heavy-Ion group, specially for my last experiment. Drs.R.Ledoux and J.Wiggins were very helpful during the last data collection. Husain Al-Juwair ,W.R.Wan_Yusoff, and J.P.Theiler were helpful in the first few runs.

I wish to thank George Yarworth for his technical assistance in every trouble I ran into. Anthony Luongo for his good targets, and Edward Drucek for his best help in remaking the time-of-flight table and adjusting it for BNL beam line.

In the end, I would like to thank Dr.M.M.Al-Kofahi for his great help during the data collection, in preparation of the thesis, and in many other instances. Dr.J.Karp and Stuart B.Gazes discussions have been very fruitful during data analysis. Thanks to Andrew Smith (Andy-sem...) for his full assistance in programing and data corrections.

FIGURE CAPTIONS:

Figure 1. A classical picture of heavy ion interactions showing the trajectories corresponding to distant, grazing, and close collisions. (W.Norenberg, J.Phys.Paris 37,C5-141,1976)

Figure 2. Continuum energy spectra of the reaction products of $^{14}\text{N} + ^{92}\text{Mo}$ at 97 MeV with single-step direct analysis fits.

Figure 3. The distribution of the excitation energy of the $^{232}\text{Th} (^{16}\text{O}, ^{12}\text{C})$ transfer reaction and its surprisal as a function of E^* . Solid line corresponds to the distribution whose surprisal is exactly linear.[2]

Figure 4. The kinematics of a two-body collision.

Figure 5. The energy distributions and the surprisal functions for projectile-like products observed at the grazing angle of 70° in $^{16}\text{O} + ^{232}\text{Th}$ reaction at 105 MeV. The curves show the most probable distributions given one constraint on the average excitation energy.[3]

Figure 6. Same as above for two constraints on the average excitation energy and the squared energy transfer.[3]

Figure 7. Same as above for two constraints on the average excitation energy and its square root.

Figure 8. Time-of-Flight experimental setup.

Figure 9. A schematic cross section of a combination of the proportional wire counter and the silicon surface barrier detector,[8]: (a) window frame, (b) front cover plate, (c) surface barrier detector, (d) microdot-to-microdot bulkhead

feedthrough, (e) anode wire, (f) window.

Figure 10. E_T versus ΔE contour plot for the $^{16}\text{O} + ^{205}\text{Tl}$ grazing reaction at 98 MeV and 70 Deg.

Figure 11. Carbon foil channel plate schematic [9].

Figure 12. Time-of-Flight electronic setup and data interface configuration.

Figure 13. ΔE versus drift. a) before the correction, b) after the linear correction

Figure 14. E_T versus ΔE contour plots for ^{16}O on ^{197}Au and on ^{205}Tl grazing reactions at 98 MeV and 70°.

Figure 15. E_T vs. E_T^2 contour plots for the above reactions.

Figure 16. The energy distributions and surprisal functions for projectile-like products observed at the grazing angle of 70° in $^{16}\text{O} + ^{205}\text{Tl}$ reaction at 98 MeV. The curves show the most probable distributions given one constraint on the average excitation energy.

Figure 17. Same as above for $^{16}\text{O} + ^{197}\text{Au}$ system.

Figure 18. The effective optimal Q-value for ^{16}O on ^{205}Tl reaction as a function of ΔN .

Figure 19. Same as above for ^{16}O on ^{197}Au reaction.

Figure 20. The most probable effective Q-value as a function of transferred nucleons for several reactions.[10]

Figure 21. The energy-integrated yield, which is proportional to the branching ratio, is plotted as a function of the number of steps ΔN , for $^{16}\text{O} + ^{205}\text{Tl}$ reaction.

Figure 22. Same as above for $^{16}\text{O} + ^{197}\text{Au}$ reaction.

Figure 23. Two-component analysis for ^{15}N , ^{17}O , ^{18}O exit channels for the above reactions.

LIST OF TABLES

Table 1 : The information contents of the experimental distributions relative to the theoretical ones for one-constraint fit (as a function of $\langle E^* \rangle$), the Lagrange parameters, $\langle E^* \rangle$, the ground state Q-value, the effective optimal Q-value for $\langle E^* \rangle$, the optimal excitation energy, the effective optimal Q-value for E_{opt}^* , and its corresponding Lagrange parameters for the grazing reaction of the $^{16}_{O+}^{197}Au$ system at beam energy of 98 MeV and the grazing angle of about 70 degrees.

Table 2 : Same as above for the $^{16}_{O+}^{205}Tl$ system.

Table 3 : Total energy-integrated yield and the contribution of each components are listed for different projectile like products.

REFERENCES:

- [1]. T. Udayama, B. T. Kim, T. Tamura, proceedings of the IPCR symposium on macroscopic features of heavy-ion collisions and pre-equilibrium process, Hacone, sept. 1977, edited by H. Kamitsubo, M. Ishihara (IPCR Cyclotron Progress Report, Wako-Shi, Saitama, 1977).
- [2]. R. D. Levine, S. G. Steadman, J. S. Karp, Y. Alhassid, Phys. Rev. Lett. 41, 1537 (1978).
- [3]. J. S. Karp, S. G. Steadman, S. B. Gazes and R. Ledoux, and F. Videbaek, submitted to Phys. Rev. C.
- [4]. Y. Alhassid, R. D. Levine, J. S. Karp, S. G. Steadman, Phys. Rev. C 20, 1789 (1979).
- [5]. R. Bass, NUCLEAR REACTIONS WITH HEAVY IONS, Berlin Heidelberg New York, Springer-Verlag, 1980 P. 3-9.
- [6]. T. Mikumo, I. Kohno, K. Katori, T. Motobayashi, S. Nakajima, S. Yoshine, H. Kamitsubo, Phys. Rev. C 14, 1989 (1976).
- [7]. A. Bohr, B. R. Mottleson, NUCLEAR STRUCTURE, New York, Benjamin (1969), vol. I, pp. 281-293.

[8].R.G.Markham, S.M.Austin and H.Laumer, Nucl.Inst.and Meth.129,141(1975).

[9].Channel plate with carbon foil designed by H.Weigner (BNL, Upton, N.Y)

[10].T.Mikomo, I.Kohno, K.Katori, T.Motobayashi, S.Nakajima, S.Yoshine, and H.Kamitsubo, Phys.Rev.C14,1458(1976).

I- INTRODUCTION

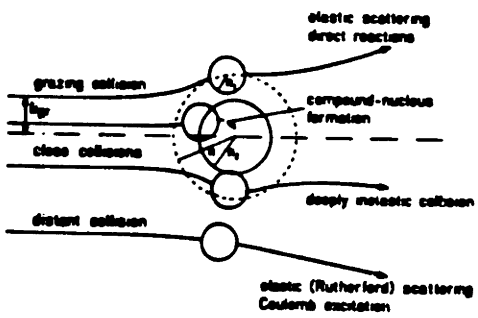
This thesis is a study of structure effects in nucleon transfer to the continuum by a light heavy ion projectile on a heavy target nucleus. The analysis of the data is in terms of a constrained phase-space approach. The selected systems for study by this work are an ^{16}O beam with an energy well above the Coulomb barrier on ^{197}Au and ^{205}Tl targets with ejectiles observed about the grazing scattering angle. After few nucleon transfer to the target one can reach $Z=82$ closed shell nuclei and see if there is any effect due to this nuclear structure. The first section of this thesis is a discussion of previous related experiments and the relevant kinematics of such energetic reactions. The second part is a review of constrained phase-space and maximal entropy formalism, nuclear level density and optimal Q -value. In the third section, the experimental technique is discussed and in the fourth section the data analysis from surprisal analysis is presented.

I-A. BACKGROUND:

In this section is a discussion of a process which is known as heavy-ion transfer reaction. In this kind of

reaction several nucleons may be transferred between the projectile and the target. Still the time scale is much shorter than compound nucleus formation ($\sim 10^{-21} \rightarrow 10^{-22}$ sec.). In general, for a light projectile bombarded on a heavy target, the measured light ejectiles are close in mass and charge to the original projectile. In other words, the exit channel retains "memory" of the entrance channel unlike with compound nucleus formation. The former reaction happens for impact parameters and at an energy such that the projectile grazes the target at a distance for outer nuclear wave functions, or nuclear surfaces, to overlap slightly. Distant collision, with large impact parameters, lead primarily to elastic (Rutherford) scattering, tunneling, or Coulomb excitation. Close collisions, with small impact parameters, lead to deeply inelastic collision or compound nucleus formation. A classical picture of heavy-ion interactions showing the trajectories corresponding to distant, grazing, and close collision is shown in figure 1.

Transfer reactions can be understood within the framework of the distorted wave Born approximation (DWBA). Udagawa et al [1] have applied a multi-step direct reaction theory, using a DWBA cross-section, to such heavy-ion transfer. In this way of treating transfer reactions the cross-sections of the various processes (1-step, 3-step,...) sum up to yield the observed cross-section. In figure.2 the

**FIGURE 1**

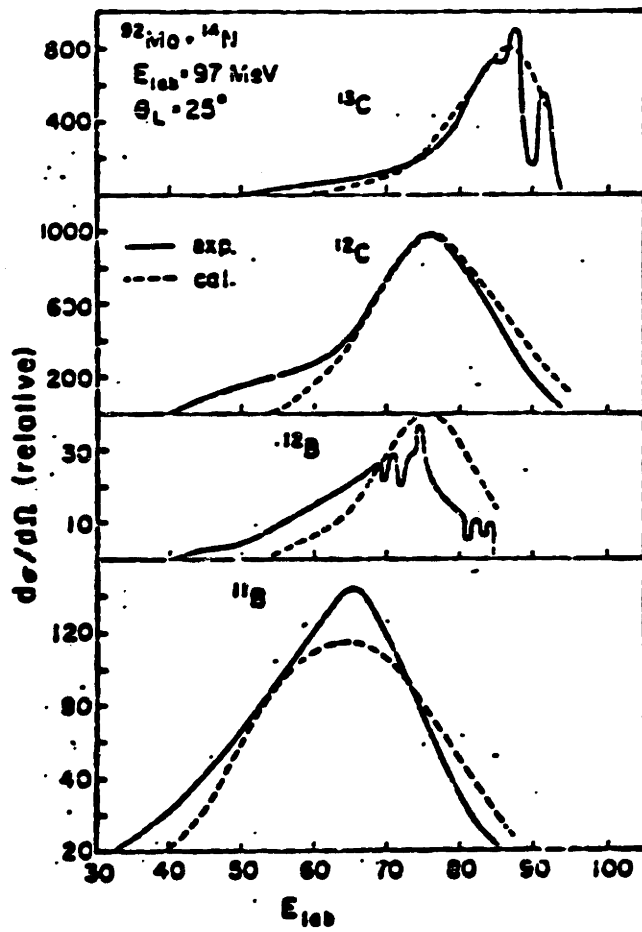


FIGURE 2

experimental spectra of the ejectiles from the reaction $^{14}\text{N} + ^{92}\text{Mo}$ at 97 MeV, i.e., ^{13}C , ^{12}C , ^{12}B , and ^{11}B measured at 25 degrees are shown by the solid curves. The dashed curves indicate the 1-step process calculations which reproduce the peak positions and width of the energy spectra, but consistently underestimate the cross-sections in the region of high excitation. This is likely due to neglect of higher order processes.

Often, many features of heavy-ion transfer reactions appear to be particular to individual reactions; whereas, in fact, many are general characteristics which depend on the angular momentum and energy of the system rather than the specific nature of the interacting nuclei. For example, the amount of angular momentum and the incident energy above the Coulomb barrier cause the angular distributions and energy spectra of deep inelastic collisions to change considerably, although the reaction mechanism does not necessarily change. Furthermore, the excitation level density of the heavy nuclei in the continuum region is so dense that the average population is considered an important factor, independent of the structure of the individual eigenstate.

A formalism has been developed which treats the population of the states of the system as the most statistical possible subject to certain physical

time-dependent constraints. The distribution of final states are then that of maximum entropy or least information content. Such a method has been highly successful in predicting energy spectra of specific ejectiles, as shown in figure 3 for the $^{16}\text{O} + ^{232}\text{Th}$ system at 105 MeV incident energy. [2,3].

In this thesis, measurements of excitation energy spectra for the various ejectiles X in the $^{205}\text{Tl} (^{16}\text{O}, X)$ and $^{197}\text{Au} (^{16}\text{O}, X)$ reactions at the grazing angle have been obtained using a time-of-flight spectrometer. These energy distributions are then compared to those of maximal entropy subject to one or two constraints. This comparison is made for reactions of highly asymmetric systems of lighter projectiles on heavier targets, with target masses near to close shell ($Z=82$) nuclei. This is in order to study effects of structure on the reactions when the mass number of the heavy ejectile becomes equal or more than closed shell nuclei. The reason for selecting highly asymmetric systems, such as $^{16}\text{O} + ^{197}\text{Au}$ or $^{16}\text{O} + ^{205}\text{Tl}$ is that for final average excitation energy of about 18 MeV, the light oxygen-like ejectile would accordingly only acquire 1 MeV average excitation energy, if the energy were distributed according to mass. This is expected because the heavier nucleus has a much higher level density or many more degrees of freedom. Thus, the light ejectile does not have enough energy (about 8 MeV needed) to evaporate a particle before it is measured. The

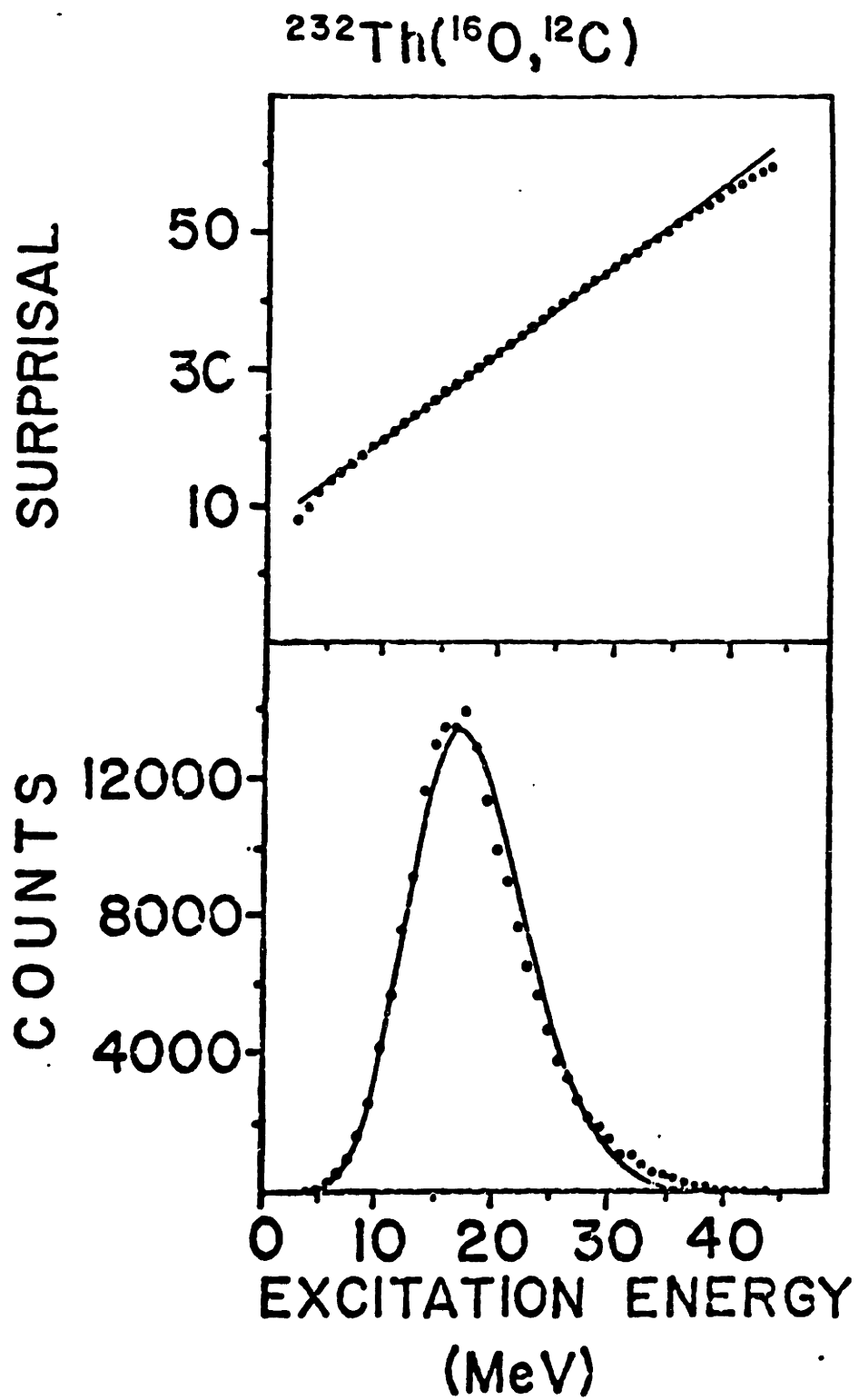


FIGURE 3

transfer reaction remains a 2-body problem: the heavier ejectile's energy, mass, and charge are all determined by the measured properties of the light ejectiles.

The grazing reactions $^{16}_{0+}^{197}\text{Au}$, and $^{16}_{0+}^{205}\text{Tl}$ were selected for study because of the mass asymmetry and being very close to the closed shell nucleus ^{82}Pb . They also exhibit a surprisingly large amount of energy damping despite having only a few partial waves contributing to the transfer cross-section. For 1- or 2-nucleon transfer, up to about one-half the incident kinetic energy above the barrier is dissipated into internal energy, while for 5- or more nucleon transfer, almost all is dissipated. The effect of the transferred energy can be isolated from that of transferred angular momentum. Only a relatively modest amount of angular momentum is transferred, which imparts a small rotational energy to the heavy nucleus compared to the initial excitation energy.

The bombarding energy (98 MeV) chosen for the measurements is such that the projectile can graze the target at the forward angle. If the energy is very near to the Coulomb barrier, the "grazing" orbit would have a sharp turning point and brief interaction time. This would not allow many nucleon transfer. On the contrary, if we have a very high energy beam, then the grazing angle would be very far

forward, where the transferred groups would be cotaminated by a large tail from the elastic peak. Furthermore, more deeply penetrating fully damped collisions would dominate. The energies are chosen to obtain a grazing angle of 70° in order to maximize the few-nucleon grazing process.

The measured energy distributions are compared with those of maximal entropy. To identify the dominant constraint it is useful to compare the measured distribution with the statistical or uniform distribution as a function of a relevant physical variable. The logarithmic ratio of the experimental to statistical distribution, the surprisal function, as a function of energy gives the deviation of final state probability from the statistical one [3]. As will be shown later, observation of a linear surprisal indicates that the energy variable is then the one that is constrained. This description of the data is referred to as surprisal analysis [4]. In general, with more than one constraint, one expects that the distribution of states of the system will evolve in time such that it will be of maximal entropy, but consistent with the time-dependent constraints imposed by the dynamics of the reaction. In other words, the observed distribution is the one which is least biased, or contains the least information content, and yet still satisfies the constraints. The internal states of the heavy nucleus are dense enough, so that the Fermi gas model has been used to

approximate the nuclear level density, or phase-space. Constraints are physically meaningful as suggested by the observed dependence of the surprisal on the excitation energy. This indicates the utility of the maximal entropy approach in order to understand the reaction mechanism. Within this framework one can then see if significant deviations from the average behavior occur which might be due to nuclear structure.

I-B. SCATTERING OF HEAVY-IONS AS SEMICLASSICAL OBJECTS:

The kinematic calculation for heavy-ion collisions can be treated in terms of a classical trajectory by using energy and momentum conservation in addition to conservation of nucleon number:

$$(I-1) \quad A_1 + A_2 = A_3 + A_4,$$

where A_1 , A_2 , A_3 , and A_4 are nucleon numbers for projectile, target, light ejectile, and heavy ejectile, respectively. The reaction Q -value is defined as the difference of the final and initial kinetic energies:

$$(I-2) \quad Q = E_f - E_i = E_3 + E_4 - E_1,$$

where for elastic collisions $Q=0$, for exoergic reactions, where energy is released, $Q>0$, and for endoergic reaction,

where kinetic energy is absorbed, $Q < 0$. For transfer reactions the Q -value is generally negative, since the incident kinetic energy is converted into internal excitation, or heat, by frictional forces during the time of contact. So, the Q -value can be expressed as

$$(I-3) \quad Q = Q_0 - E^*$$

where Q_0 is the difference of the initial and final masses,

$$(I-4) \quad Q_0 = (M_1 + M_2 - M_3 - M_4) c^2$$

and E^* is the internal excitation energy in the final state.

A schematic diagram of a two-body collision is given in figure 4. Initial particles 1 and 2 have velocities v_1 and 0 in the lab system, while final particles 3 and 4 have velocities v_3 and v_4 in the lab system and v_3' , v_4' with respect to the center-of-mass system. v is the center-of-mass velocity, θ is the scattering angle of light particle 3, and ψ is the scattering angle (in lab system) for heavy particle 4.

To calculate the Q -value we use energy and momentum conservation, where

$$E_1 + (M_1 + M_2) c^2 = (M_3 + M_4) c^2 + E_3 + E_4$$

$$(I-5) \quad \vec{P}_1 = \vec{P}_3 + \vec{P}_4$$

\vec{P}_1 , \vec{P}_3 , \vec{P}_4 are the corresponding momenta for particles 1, 3, 4

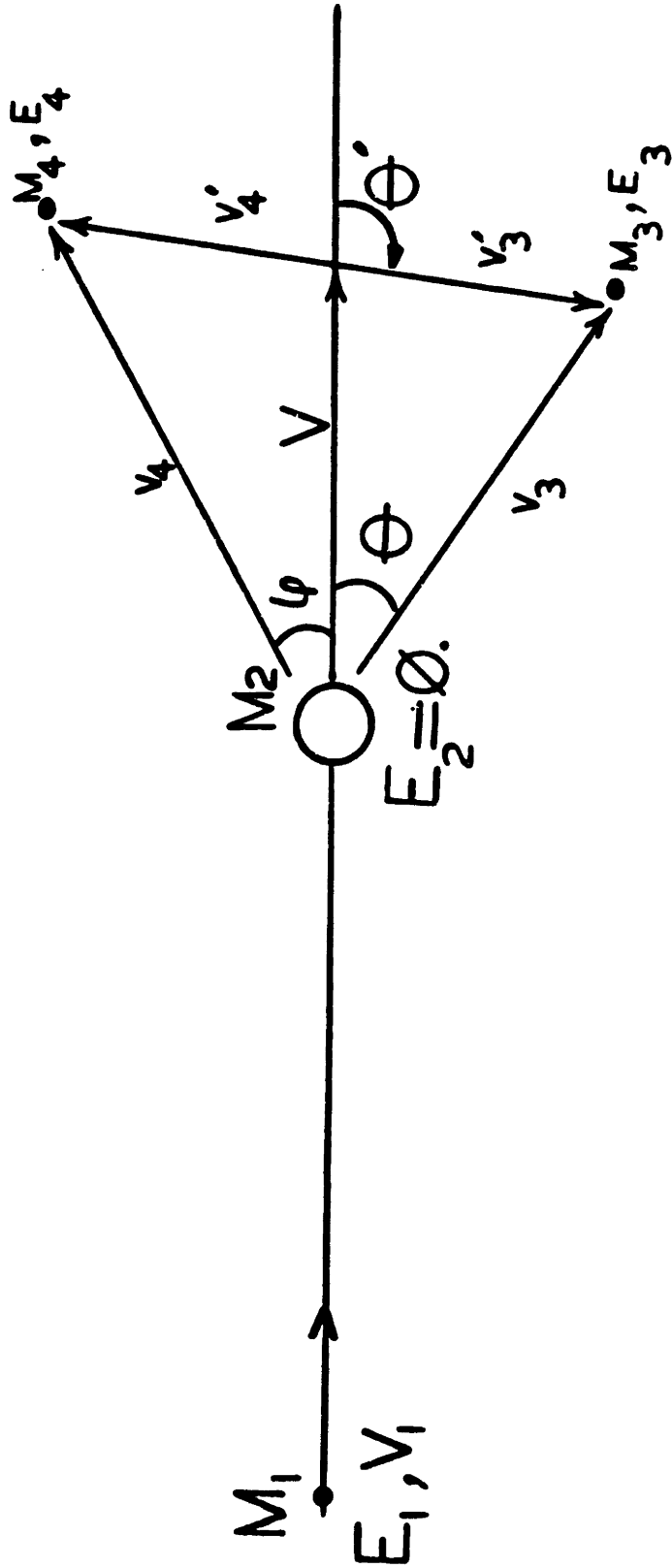


FIGURE 4

and also we have

$$(I-6) \quad P^2 = 2 m E.$$

By using equations I-2, I-5, I-6 one gets

$$(I-7) \quad Q = \frac{P_3^2}{2M_3} + \frac{P_1^2 + P_2^2 - 2P_1P_2 \cos \theta}{2M_4} - \frac{P_1^2}{2M_1}$$

or

$$(I-8) \quad Q = E_3 \left(1 + \frac{M_3}{M_4}\right) - E_1 \left(1 - \frac{M_1}{M_4}\right) - 2 \left(\frac{M_1 M_3 E_3 E_1}{M_4^2} \right)^{1/2} \cos \theta,$$

where $Q=0$ for elastic scattering and $M_1 = M_3$, $M_2 = M_4$. Then, equation (I-8) becomes

$$(I-9) \quad \frac{E_3}{E_1} = \left(\frac{M_1}{M_1 + M_2} \right)^2 \left[\cos \theta + \left\{ \left(\frac{M_2}{M_1} \right)^2 - \sin^2 \theta \right\}^{1/2} \right]^2, \quad \frac{E_3}{E_1} < 1.$$

Kinematic calculations can be expressed in terms of the center-of-mass frame too [5]. In the center of mass system the two ions move with initial velocities v_1' and v_2'

$$(I-10) \quad v_1' = \left(A_2 / (A_1 + A_2) \right) v_1, \quad v_2' = \left(A_1 / (A_1 + A_2) \right) v_2;$$

and the kinetic energy and relative momentum are

$$\frac{E_{CM}}{M} = 0.5M (A_1 v_1'^2 + A_2 v_2'^2) = 0.5uv$$

$$(I-11) \quad P = M (A_1 v_1' + A_2 v_2') = uv,$$

where M is the nucleon mass and u denotes the reduced mass

which is given by

$$u = M_1 A_1 A_2 / (A_1 + A_2).$$

Using (I-11) one can write a relationship between the energy of the incident particle in the center-of-mass (C.M.) and laboratory systems:

$$E_{C.M.} = 1/2 u v_1^2 = (M_2 / (M_1 + M_2)) E_1$$

and the final energy in the C.M. system can be written as

$$(I-12) \quad E_{F,C.M.} = 1/2 u v_{FF}^2 = E_{C.M.} + Q_0$$

The above approximation results because the final C.M. system is not the same as the initial C.M. frame due to mass transfer. However, the error is small for $A_1 \ll A_2$.

The emission angle of the light fragment with respect to the incident beam direction, θ (in the lab system) and θ' (in the C.M. system), is given by

$$(I-13) \quad \tan \theta = \frac{v_2' \sin \theta'}{v_3' \cos \theta' + v_{C.M.}} = \frac{\sin \theta'}{\cos \theta' + v_3^*}$$

where $v_{C.M.} = v_2' = \frac{A_1}{A_1 + A_2} v_1$

$$(I-14) \quad v_3^* = \frac{v_{C.M.}}{v_3'}$$

In the special case of elastic scattering (or, more generally, in collisions with negligible mass and energy transfer), the magnitude of the C.M. velocity is not changed, and hence we obtain from equations (I-10), (I-14), and

$$(I-13), \quad v_3^* = \frac{v_{C.M.}}{v_3'} = \frac{A_1}{A_2}.$$

In the general case of a two-body reaction with product mass numbers A_3 and A_4 , the quantity is given by [5]

$$V_3 = + \left(\frac{A_1 A_3}{A_4 A_2} \cdot \frac{E_{C.M.}}{E_{C.M.} + Q} \right)^{1/2}$$

where Q is the Q -value in equation I-8.

In general, for transfer to happen we need to overcome the Coulomb barrier. Very often, this barrier is a large fraction of the incident energy. After the reaction, when the particle is ejected from the di-nuclear system, the energy is retrieved and the Coulomb energy is converted back into kinetic energy of the ejectile. If protons are transferred, then the energy retrieved will be different than the energy for overcoming the barrier. This energy difference is already accounted for in the Q -value, such that

$$(I-16) \quad Q_{eff} = Q + \Delta V_C,$$

where ΔV_C is the difference between the initial and the final Coulomb energies. The Q_{eff} is interpreted to be the transferred energy due to the reaction where the Coulomb difference has been subtracted out. The Coulomb energy for the initial and final channels and the difference can be written as

$$(I-17) \quad V_{Ci} = \frac{Z_1 Z_2 e^2}{R_1 + R_2}, \quad V_{Cf} = \frac{Z_4 Z_3 e^2}{R_3 + R_4}, \quad \Delta V_C = V_{Ci} - V_{Cf},$$

where R_L is the nuclear radius

$$R_L = 1.4 A_L^{1/3} \text{ fm.}$$

One useful empirical relationship is that between average energy transfer and number of transferred nucleons ΔN . Specifically, it has been noted by Mikumo et al [6], that the relationship is linear,

$$(I-18) \quad \langle Q_{EFF} \rangle = \alpha_{EFF} \Delta N + \beta_{EFF}$$

and ΔN is restricted to $\Delta N \leq 4$ or 5. This has been developed by Y. Alhassid et al. [4], who have shown that approximately

$$(I-19) \quad \begin{cases} \langle Q_{EFF} \rangle = [(\cos^2 \beta) \exp(-\kappa \sin^2 \beta) - 1] \cdot E_{C.M.} \\ \cos^2 \beta = (1 - m/A_1 - n/A_2)(1 - m/A_3 - n/A_4). \end{cases}$$

Here, m is the number of nucleons transferred from projectile to target, n is the number of nucleons transferred from target to projectile, κ is a fit parameter. Knowing $\langle Q_{EFF} \rangle$ one can then determine the average excitation energy of the system

$$(I-20) \quad \langle E^* \rangle = Q_0 + \Delta V_C - \langle Q_{EFF} \rangle.$$

This $\langle E^* \rangle$ will be shown to be the dominant constraint of the reaction (figure 3).

II - SURPRISAL ANALYSIS:

Consider the measurable states of the system to be divided into groups with index i . Denote the probability of occupying the i^{th} group as P_i , which is proportional to the fraction of final states that belong to that group of states. Let P be the observed distribution of those groups of states. Then, the entropy of the probability distribution is

$$S = - \sum_i P_i \ln P_i,$$

where the sum is over the number of groups. For a system with $\rho(x)$ as the density of states we have

$$\int \rho(x) dx = N,$$

where N is the number of possible final states. We can write

$$\rho^{\circ}(x) = \rho(x) / N$$

as the "prior" probability density (assuming each state is equally likely to be occupied) for the system to be in a state described by x .

This distribution with entropy S_0 is the one for which the available phase-space would be uniformly populated in the absence of constraints. The information content is defined as

$$S = S_0 - S = \sum_i P_i \ln (P_i / P_i^{\circ}).$$

Maximizing the entropy S is equivalent to minimizing the information content, which determines the distribution of maximal entropy to be

$$P^{ME} = P^0 \exp\left[-\lambda_0 - \sum_{r=1}^n \lambda_r A_r(i)\right].$$

The observable quantities A_r determine the n constraints, $\langle A_r \rangle = \sum_i P_i A_r(i)$. Hence, if the quantity known as the surprisal $-\ln(P/P^0)$ has a linear functional dependence with respect to a kinematic variable, that variable is the constraint of the distribution.

The "prior" distribution or available phase-space, with which the experimental distribution is compared, is given by a product of the internal nuclear level density $\rho_i(E^*)$ and the translational level density $\rho(E_F)$

$$\rho_i^0 = \rho(E) = \rho_i(E^*) \cdot \rho_T(E_F),$$

where E^* is the internal or excitation energy and E_F is the translational or kinetic energy. Due to the high degeneracy of nuclear states for thallium-like nuclei at excitation energies more than 1 MeV, the nucleus can be treated as a fully degenerate gas of independent fermions moving in an average potential. The average initial level density is the number of ways the excitation energy can be distributed among the single-particle levels. For the case of equal number of protons and neutrons in a Fermi gas, we have

$$p(E^*) \propto u^{-2} \exp[2(au)^{1/2}]$$

where,

$$u = E^* - E_{\text{ROT}} - E_{\text{PE}} ;$$

with

$$E_{\text{ROT}} = J(J+1)\hbar^2 / 2I_{\text{ROT}} ,$$

$$E_{\text{PE}} = 12 \delta A^{-1/2}$$

and

$$\delta = \begin{cases} 0 & \text{odd-odd} \\ 1 & \text{odd-even} \\ 2 & \text{even-even} \end{cases} \quad [7] .$$

and a = nuclear level density parameter, which is proportional to the mass A . Empirically, this proportionality constant is found [10] to be $1/8$.

II-A. ONE CONSTRAINT ANALYSIS:

Consider the average energy, or centroid of the energy distribution, as the constraint. The maximal entropy distribution $p^{\text{ME}}(E^*)$ is constrained to have the same average as the experimental distribution,

$$p^{\text{ME}}(E^*) \sim d^2 \sigma / d\Omega dE^*$$

or

$$P^{ME}(E^*) = P_0(u) \exp(-\lambda_0 - \lambda_1 E^*),$$

where u is function of E_{PAIR} , E_{ROT} , and E^* .

The lagrange parameter λ_1 , for a distribution subject to one constraint, depends on the most probable energy E_{MP}^* in the following manner [2]

$$\lambda_1 \approx \sqrt{a/u_{MP} - 2/u_{MP}} = \sqrt{a/(E_{MP}^* - E_{ROT} - E_{PAIR}) - 2/(E_{MP}^* - E_{ROT} - E_{PAIR})}.$$

Because the leading part is E_{MP}^* , one can estimate the value of λ_1 as

$$\lambda_1 \approx \sqrt{a/E_{MP}^*}.$$

The value of λ_1 is affected by the energy offset between u_{MP} and E_{MP}^* , although the quantitative nature of the fit is dominated by the much larger value of the most probable E_{MP}^* . Figure 5 shows distributions subject to one constraint [3].

II-B. TWO CONSTRAINT ANALYSIS:

As is clear from figure 5, the one constraint fit consistently underestimates the widths for few-nucleon transfer and overestimates the width for many-nucleon transfer. The width of the distribution for many nucleon transfer can be accounted for by constraining the variance, σ . Since

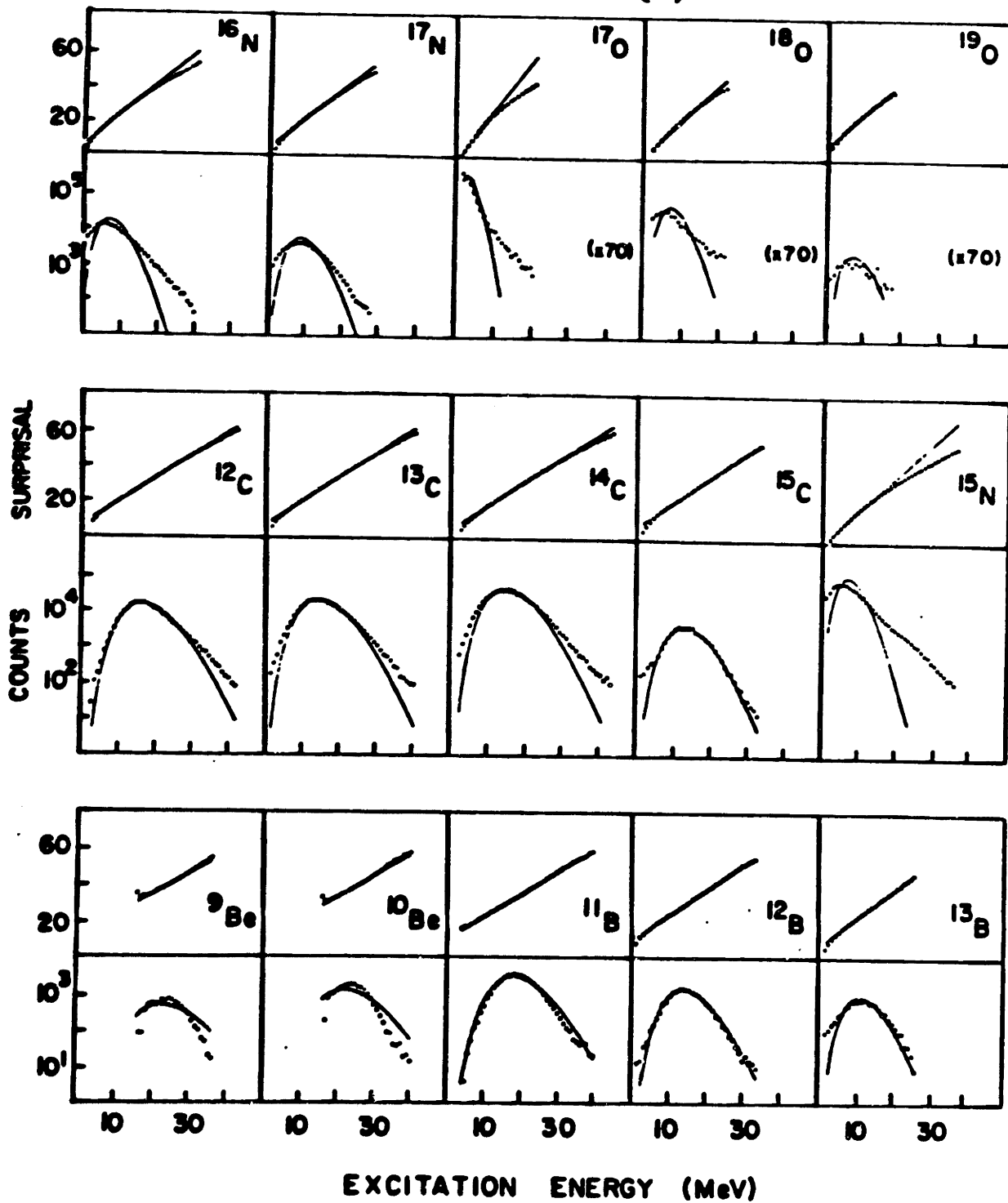
$^{232}\text{Th}(^{16}\text{O}, X)$
ONE CONSTRAINT $\langle E^0 \rangle$ 

FIGURE 5

$$(II-9) \quad \sigma^2 = \sum P(E^*) (E^* - \langle E^* \rangle)^2,$$

a constraint on the variance is equivalent to adding a second constraint on the average value of E^{*2} in addition to the first constraint on the average value of E^* [3]. Then, the distribution of maximal entropy is

$$P(E^*) = P_0(u) \exp(-\lambda_0 - \lambda_1 E^* - \lambda_2 E^{*2})$$

Figure 6 shows the resulting fits from J. Karp et al. [3], for ^9Be , ^{10}Be , and ^{11}B , for the cases of 7-, 6-, and 5-nucleon transfer, respectively.

It has been also argued [4] that there could be a different constraint acting on the system, particularly for small ΔN , where the width of the exciton distribution, rather than the width of the energy distribution, acts as the second constraint. The variance of the exciton distribution about the mean is found to be approximately $(aE^*)^{1/2}$. Therefore, $\langle E^{*1/2} \rangle$ determines the average variance of the exciton distribution.

So, the distribution of maximal entropy becomes

$$P(E^*) = P_0(u) \exp(-\lambda_0 - \lambda_1 E^* - \lambda_2 E^{*1/2})$$

where $\langle E^* \rangle$ and $\langle E^{*1/2} \rangle$ are the first and the second constraints. This procedure is illustrated in figure 7. Here, because the prior distribution depends exponentially on the

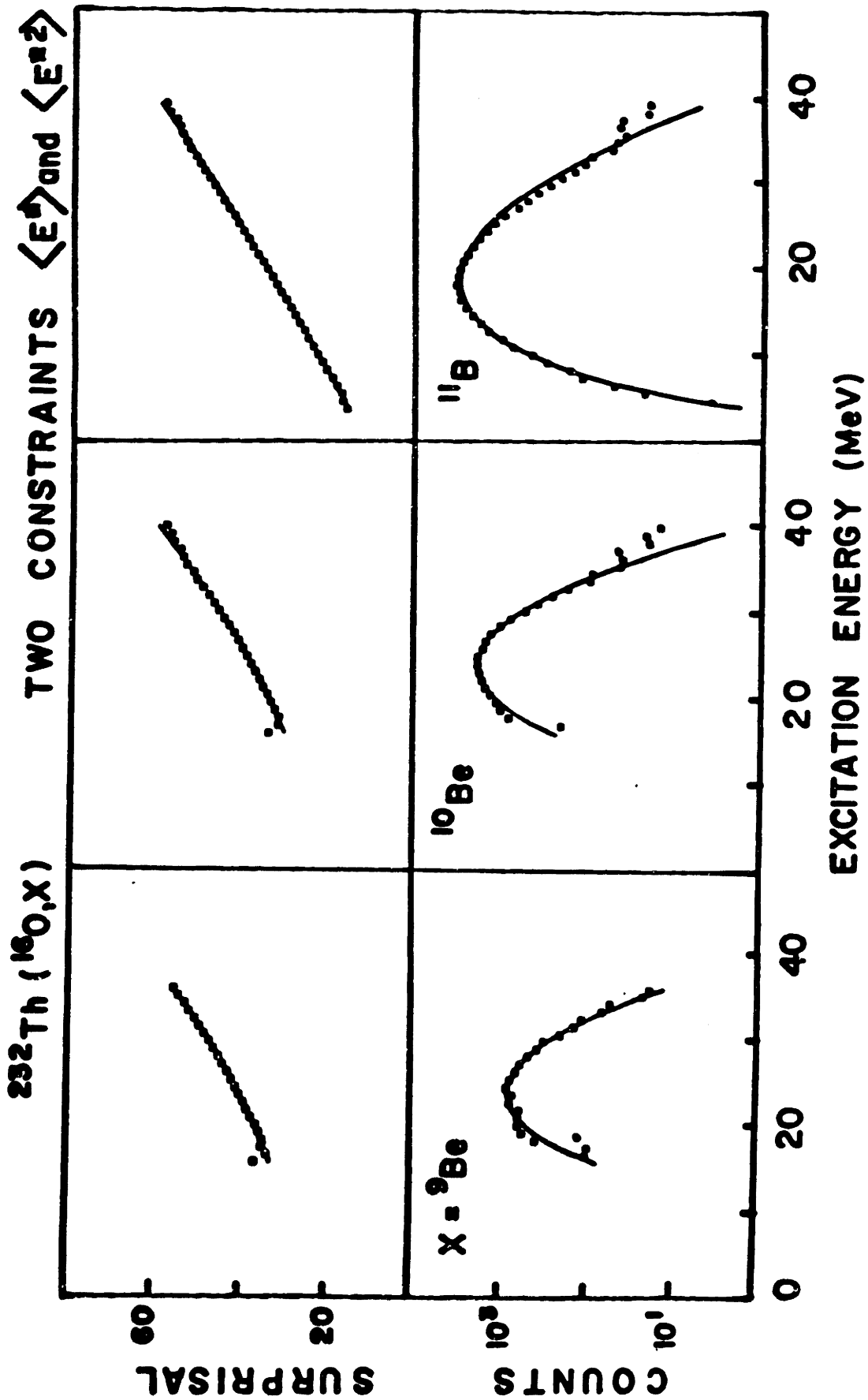


FIGURE 6

232Th(16O,X)

TWO CONSTRAINTS $\langle E^0 \rangle$ and $\langle E^{0/2} \rangle$

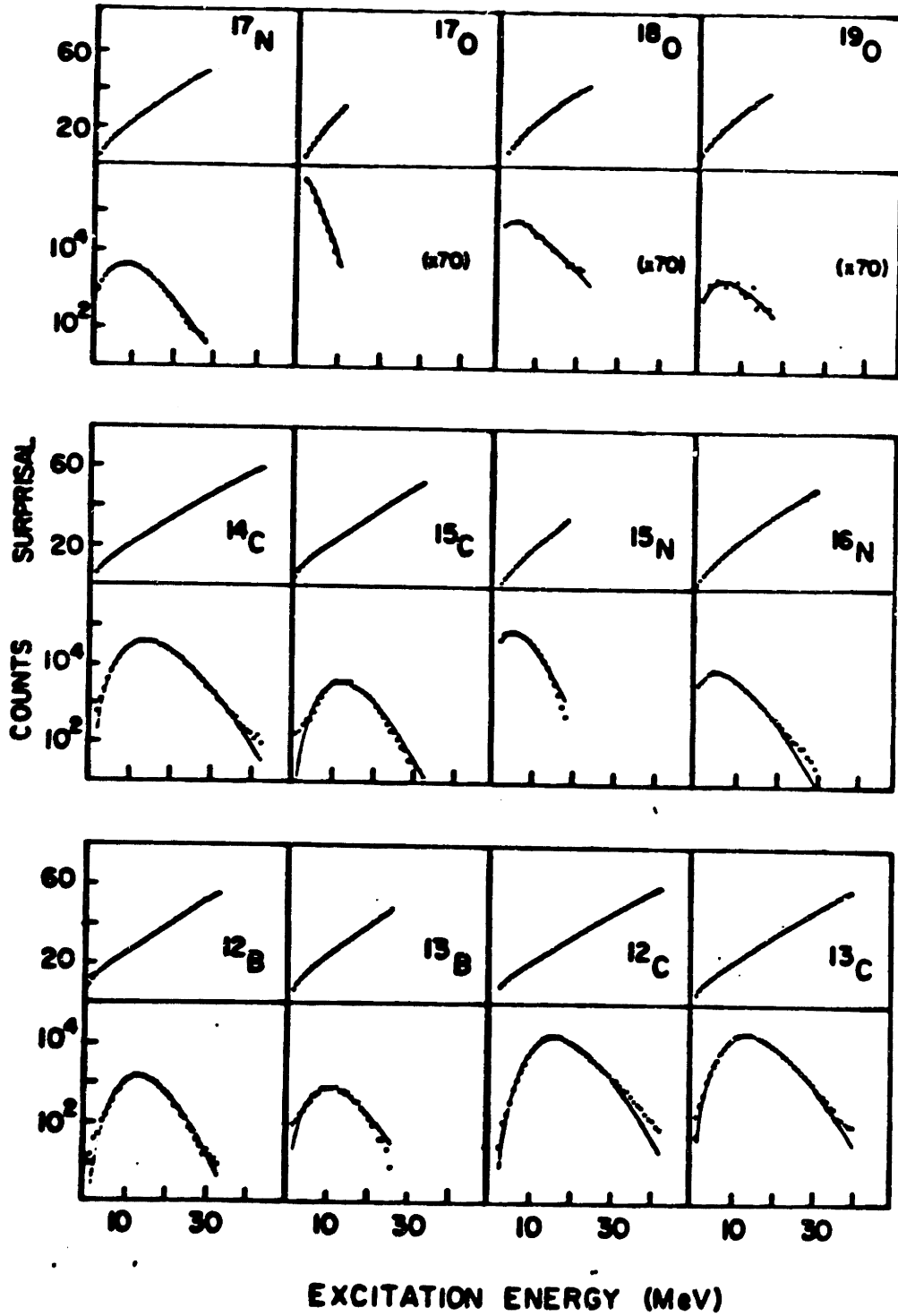


FIGURE 7

square root of E_{mp}^* , the above form of the distribution can be rewritten in the form of a one-constraint distribution [4].

If we define $a^* = (a_{mp}^* - \lambda_2/2)^2$, then

$$\lambda_1 = (a_{mp}^* / E_{mp}^*)^{1/2}$$

$$\lambda_2 = 2a_{mp}^{*1/2} - 22E_{mp}^{*1/2} / \text{FWHM}$$

or $(a_{mp}^* / E_{mp}^*)^{1/2} = 11 (E_{mp}^* / \text{FWHM})^2$

Therefore, the second constraint can be related to the relative value of the average excitation energy and the width of the distribution.

III - EXPERIMENTAL METHOD

The data for this thesis were taken by using the Tandem Van de Graaff Facility of the Brookhaven National Laboratory (BNL). An experimental setup was placed in the target room consisting of a time-of-flight arm mounted on an angular correlation table and connected to a sliding seal target chamber (figure 8). Both the charge and mass of the reaction products were measured by using a 98 MeV ^{16}O beam on ^{197}Au and ^{205}Tl targets at about the grazing angle ($\theta_{\text{Lab}} = 70^\circ$).

To determine the charge of the heavy-ion ejectiles, a counter telescope consisting of a proportional wire ΔE and solid state (silicon) E section was used, in a configuration proposed by Markham et al. [8]. A cross-sectional view is shown in figure 9. The ΔE signal is obtained from the proportional wire located within a volume of gas contained inside a conducting walled box which is held at ground potential. The E signal is obtained from a Si surface barrier detector which forms the back wall of the box. The electrons freed from gas atoms by the passage of a charged particle drift toward a 20 μm diameter nichrome metal wire to which is applied a high voltage of +560 volts. When the electrons are far from the wire they drift at nearly constant speed, about 5 cm/usec, whereas when they reach a distance of a few

TIME-OF-FLIGHT

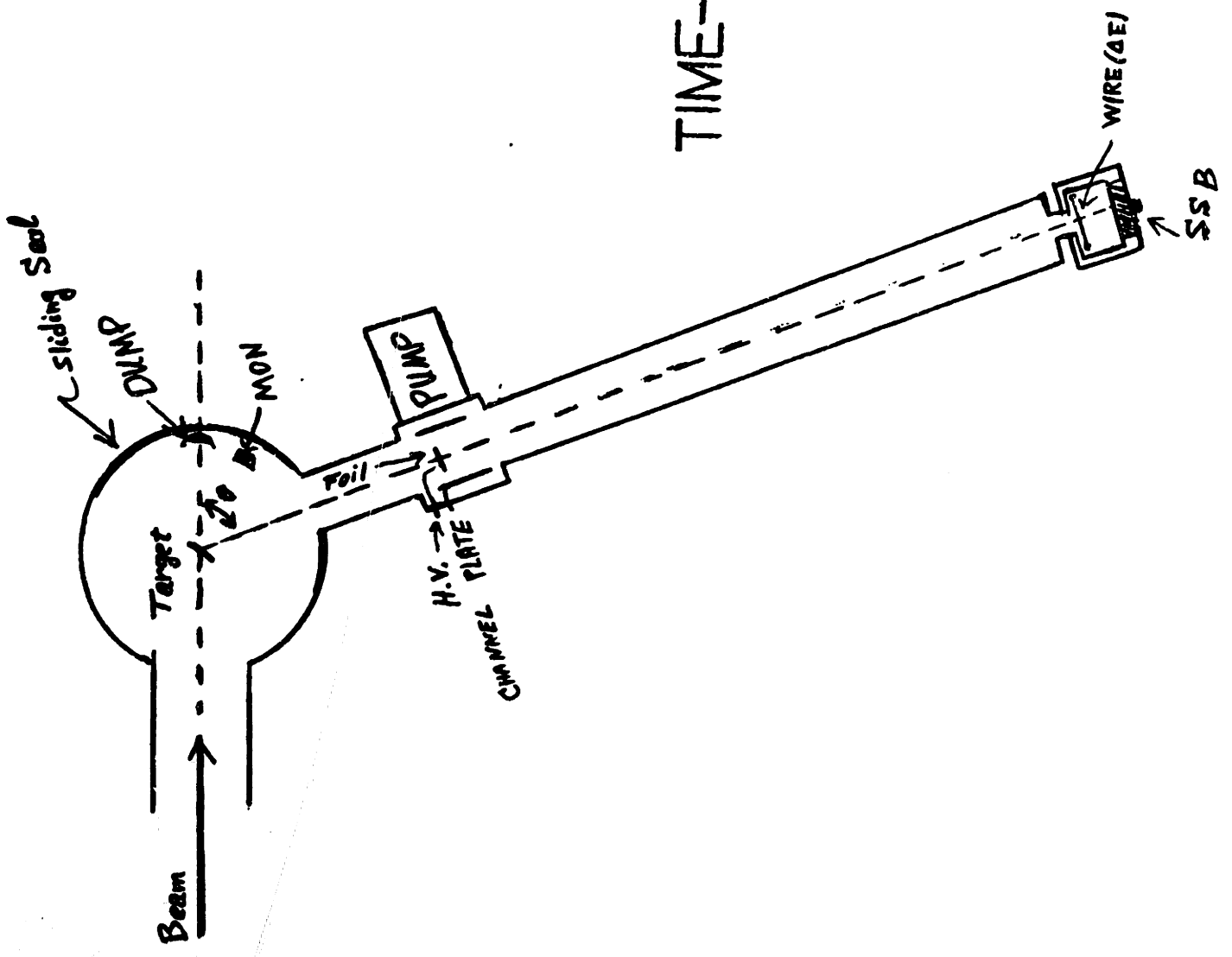


FIGURE 8

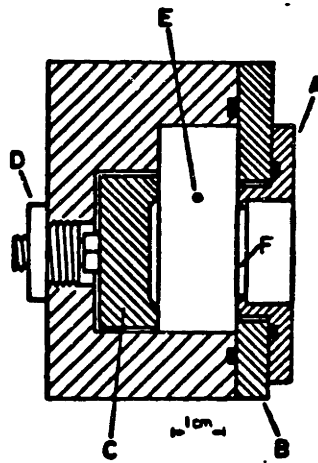


FIGURE 9

diameters from the wire the intense electric field in that region accelerates them to high enough velocities so that they can ionize other gas atoms, producing a large multiplication of the original charge produced by the ionizing nucleus. The wire used has a low resistivity.

The charge resolution of the detector was sufficient to resolve nuclei of $Z \ll 8$. The principle of the charge determination can be seen from the Bethe-Bloch formula for the stopping of a charged particle with velocity much greater than electron velocities

$$\frac{dE}{dx} = 4\pi e^4 z^2 \frac{N}{M_e v^2} \cdot Z' \left[\ln \frac{2M_e v^2}{I} - \ln(1-\beta^2) - \beta^2 \right],$$

where the term in brackets varies slowly with energy. Z is the particle's atomic number, N is the number of atoms/cm³, z' is the atomic number of the stopping material, $\beta = v/c$, and I is roughly the ionization potential of the stopping medium, which cannot be calculated exactly and is usually taken as a constant to be determined empirically for the stopping medium in question. It can be seen that $E_T - \Delta E$ is proportional to MZ^2 of the stopping ion, where E_T is the total energy of the ion. Thus, on a plot of E_T vs. ΔE different isotopes will be on hyperboli of constant MZ^2 . The mass dependence is much weaker than the Z dependence for heavy-ions of $Z \gg 4$, and thus such a map is useful principally for determining the Z of a nucleus in this experiment. It should be noted that the gas used in the counter was 99% pure isobutane at a pressure of 74 torr.

The gas was contained by a 1.9 μm thick polypropylene window which has been supported by a 0.0002" thick nickel mesh.

An example of such an E_T - ΔE plot taken with the counter used is shown in figure 10. The total energy resolution was a little more than 1% (about 1.2%), for the summed E_T signal (determined by the solid state detector). The energy calibration was obtained by measuring elastic scattering at energies of 50 and 98 MeV. The mass of the ejectile was determined from its flight time as $M \propto Et^2$. To get a good timing resolution, timing pulses were obtained from the silicon detector and from a channel plate detecting electrons emitted by a thin 20 $\mu\text{g}/\text{cm}^2$ carbon foil channel plate (figure 11). This arrangement was designed and made-by BNL [9]. The carbon foil was mounted 143 cm from the solid state detector as shown in figure 8. The timing resolution using this technique was better than 400 psec. Using the relation,

$$M = 2Et^2 / L^2$$

the mass resolution is given by

$$\Delta M/M \approx \left[\left(\frac{\Delta E}{E} \right)^2 + \left(\frac{2\Delta t}{t} \right)^2 \right]^{1/2}$$

We need to have $\Delta M/M < 3\%$ in order to separate the ejectiles. Given the $\Delta E/E \approx 1.2\%$, the value for the TOF resolution should be $\Delta t/t \leq 1.4\%$. In our experiment this value for elastic oxygen with a TOF=44 nsec., was better than 1%. The solid state detector, of 450 mm^2 area, in the counter telescope, was

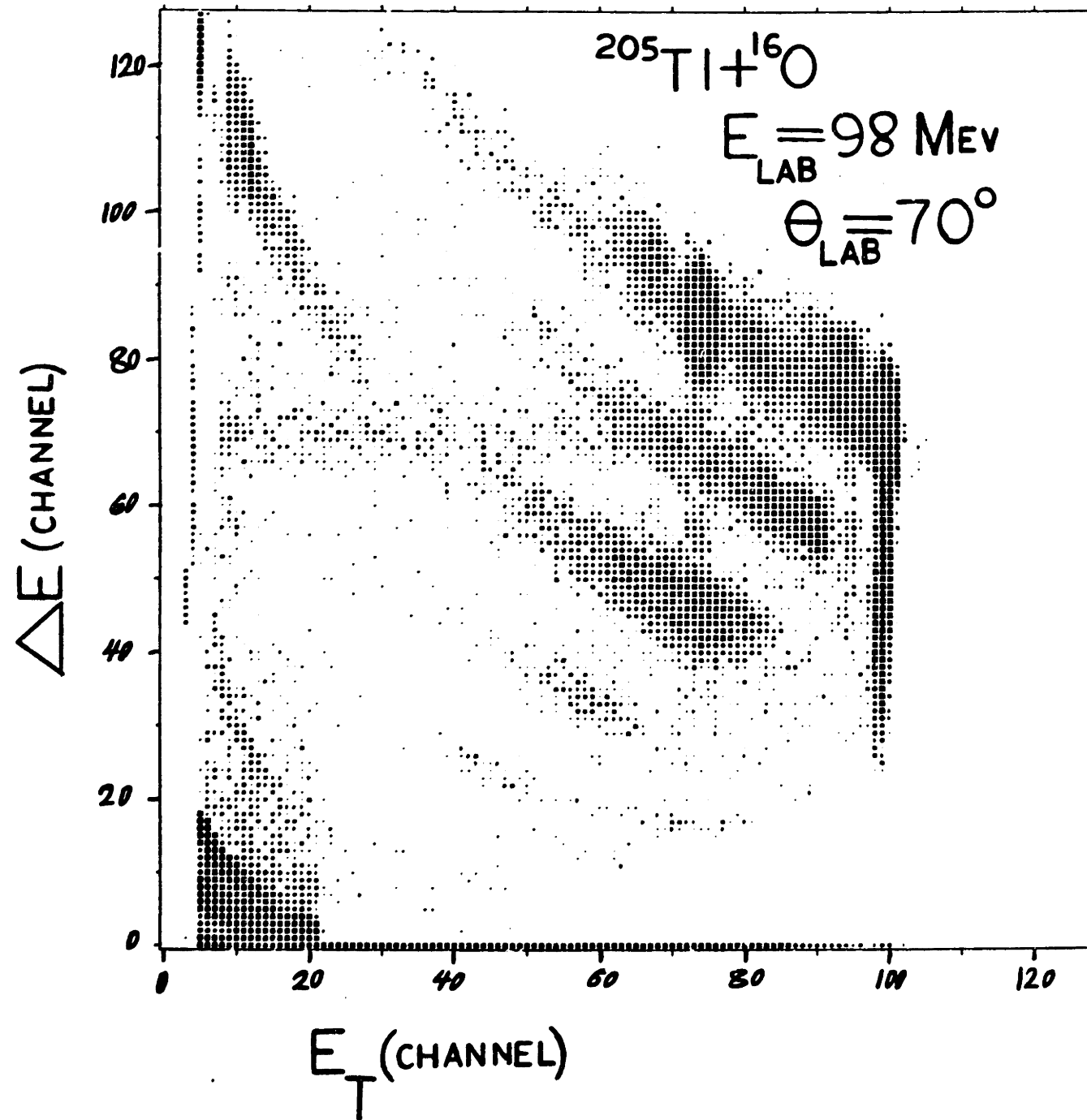


FIGURE 10

CHANNEL PLATE

MAG. PLATE

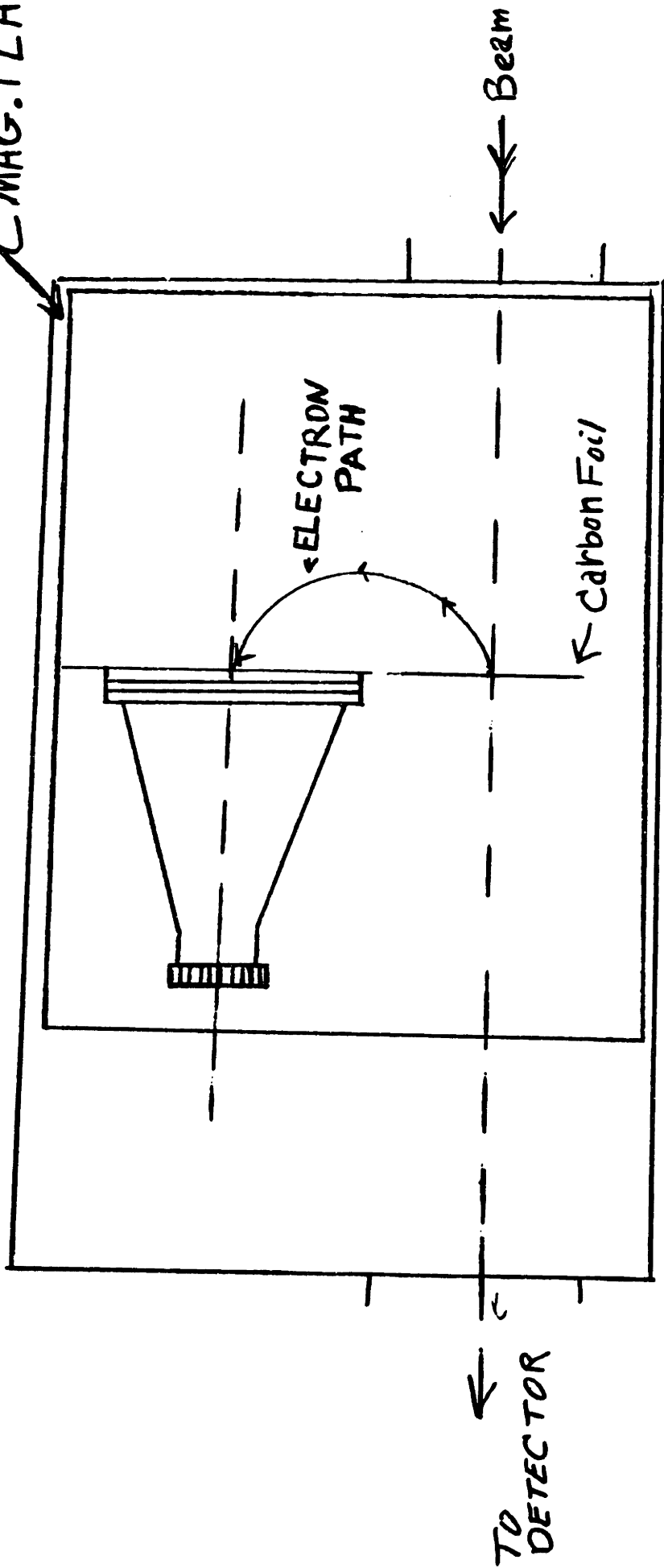
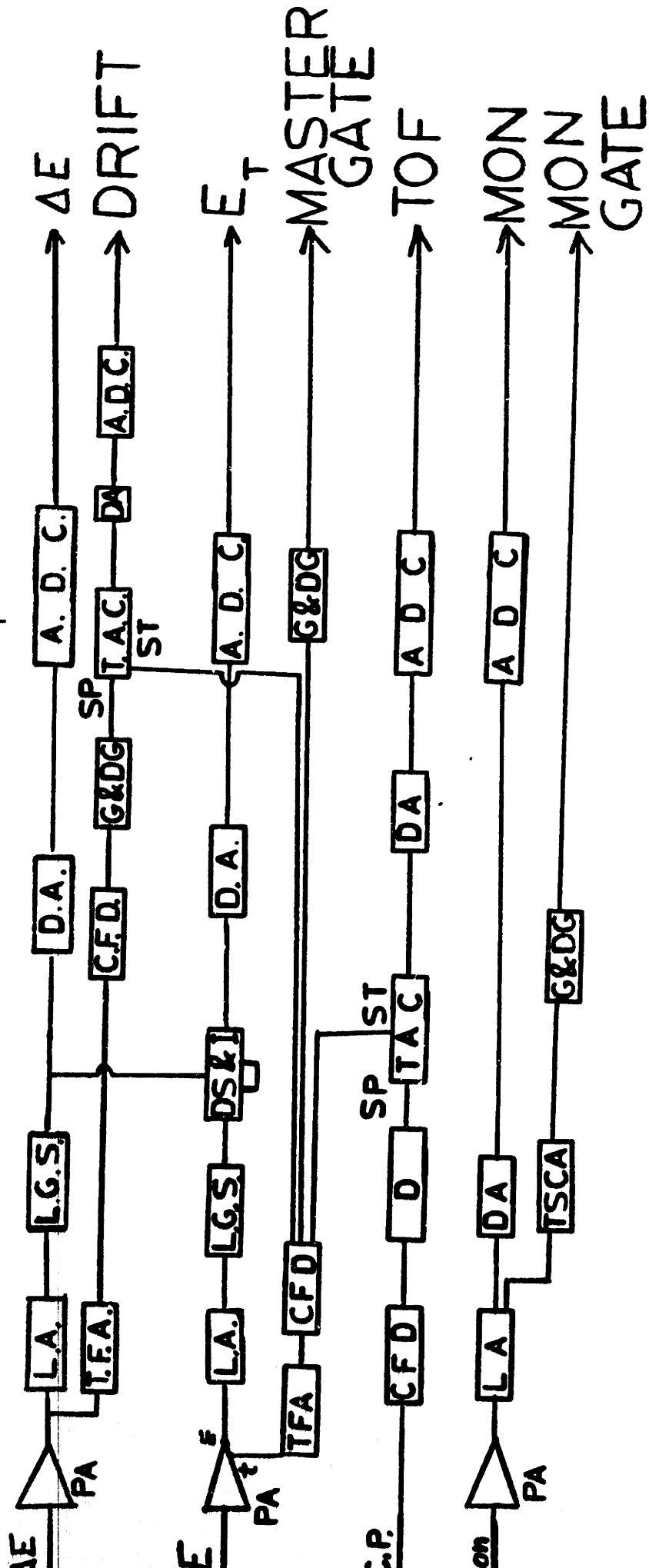


FIGURE 11

located about two meters from the target and subtended a solid angle of 0.11 msr. The carbon foil had an area of 314 mm^2 , so that the solid angle subtended by the foil was 0.8 msr. Thus the collection solid angle was determined by the solid state detector. The integrated beam current was measured by a Faraday cup in the chamber and scaled by a digital current integrator. A 50 mm^2 area and 300 μm thickness Si detector was mounted on the back wall of the chamber at $\theta_{\text{lab}}^{\text{new}} = 27$ degrees to monitor the Rutherford scattering peak at that angle (at forward angles, i.e. 27° , the elastic peaks are Rutherford scattering). So, one can monitor any change in the beam current and energy, frequently.

The electronic setup is shown in figure 12. Timing signals from the solid state detector were obtained from a fast timing output preamplifier (Canberra 2003B). Both timing signals were sent from the target area to the electronics setup in the control room using fast cable (RG-8) to minimize attenuation. To amplify the timing pulses from the SSB detector and preserve their rise time a timing filter amplifier (Ortec 454) was used with a time constant of 5 nsec. A constant fraction discriminator (QCFD) (Canberra 1428) was used to determine precisely the occurrence of the event, independent of the amplitude of the timing signal. Similarly, the timing signal from the carbon foil was processed by the QCFD. The discriminator pulses were delayed 166 nsec so that



ADC	ΔE	TOF	E _T	DRIFT	MON
EMR	16	16	16	16	1
E/E ²	2	7	7		
ΔE/E	8	7	7		
E _T		10			
THC		10			
DRIFT			10		
MON				10	
DUMP					1

LEGEND

- ADC Analog to digital converter
- CFTD Constant fraction timing discriminator
- DA Delay amplifier
- DS & I Dual sum and invert
- G & D Gate and delay
- LA Linear amplifier
- LGS Linear gate stretcher
- PA Preamplifier
- TAC Time to amplitude converter
- TSCA Timing single channel analyzer

FIGURE 12

they could be used as stop pulses for a Time-To-Amplitude convertor (TAC) (Canberra 1443A). The start pulses, from the solid state detector, have a lower count rate. The output pulses of the TAC are directly proportional to the time interval between the start and stop. The range on the TAC was set to be 100nsec.

The wire signal was fed to a proportional wire preamplifier (Canberra 2006). After amplifying and stretching the energy signals from the SSB, detector and wire, they were connected to a dual sum and inverter to obtain the total energy. The wire pulses were not only used to obtain the energy loss (ΔE) in the gas, but also used as a stop signal for a TAC. This used signals from the SSB E-detector as a start signals in order to measure the drift time of the released electrons to the wire. This information could be used later on to do correction on ΔE spectra, due to recombination.

Information on ΔE , TOF, E_T , and drift time were event mode recorded on tape for off line data analysis. Another electronic collection line was set such that one can get the ΔE signal attenuation as a function of drift time of the freed electrons in the gas. To be able to observe the mass spectra on-line, instead of E_T vs. t , which yields hyperbolic mass lines, a 128X128 spectrum was made of E_T vs. $E_T(t-t_0)^2/K$ which displays straight mass lines for easier

separation. t_0 and K are appropriate constants which are chosen such that one gets straight lines. Other event lines on the data collection interface were used for ΔE versus E_T as a 2-D 256X128 spectrum, and E_T , TAC, DRIFT, and MONITOR as 1-dimensional 1024 channel spectra. Finally the total integrated beam current was also recorded for normalization of the cross-section.

IV- DATA ANALYSIS AND RESULTS

The $^{16}\text{O}^{17}\text{Au}$ and $^{16}\text{O}^{205}\text{Tl}$ reactions at 98 MeV and $\theta_{\text{Lab}}=70$ degrees were studied to measure the spectrum of excitation energies, the effective optimal Q -values, and differential cross-section for each projectile.

As was mentioned in the previous chapter a combination of a proportional wire counter ΔE and a silicon surface barrier (SSB) detector E were used for charge (Z) identification. The mass and energy were obtained from the time-of-flight using signals from the channel plate and the SSB detector. During the experiment it was found that recombination in the proportional counter caused a large signal attenuation degrading the energy resolution of the energy loss, ΔE , signals. This effect is illustrated in figure 13, which shows the energy loss vs. the drift time. For a more energetic oxygen beam, for different values of the drift time one should have the same value for the energy loss ΔE . But as figure 13(a) shows, ΔE vs. the drift time has a slope of about 0.6 (30%) which causes the energy resolution of ΔE to be worse than 10%. By measuring the drift time of each particle, one can correct the energy loss signal, improving the energy resolution to 6.6%. It is expected that the ΔE vs. the drift time is exponential, but in this experiment an almost linear dependence was observed. So, a

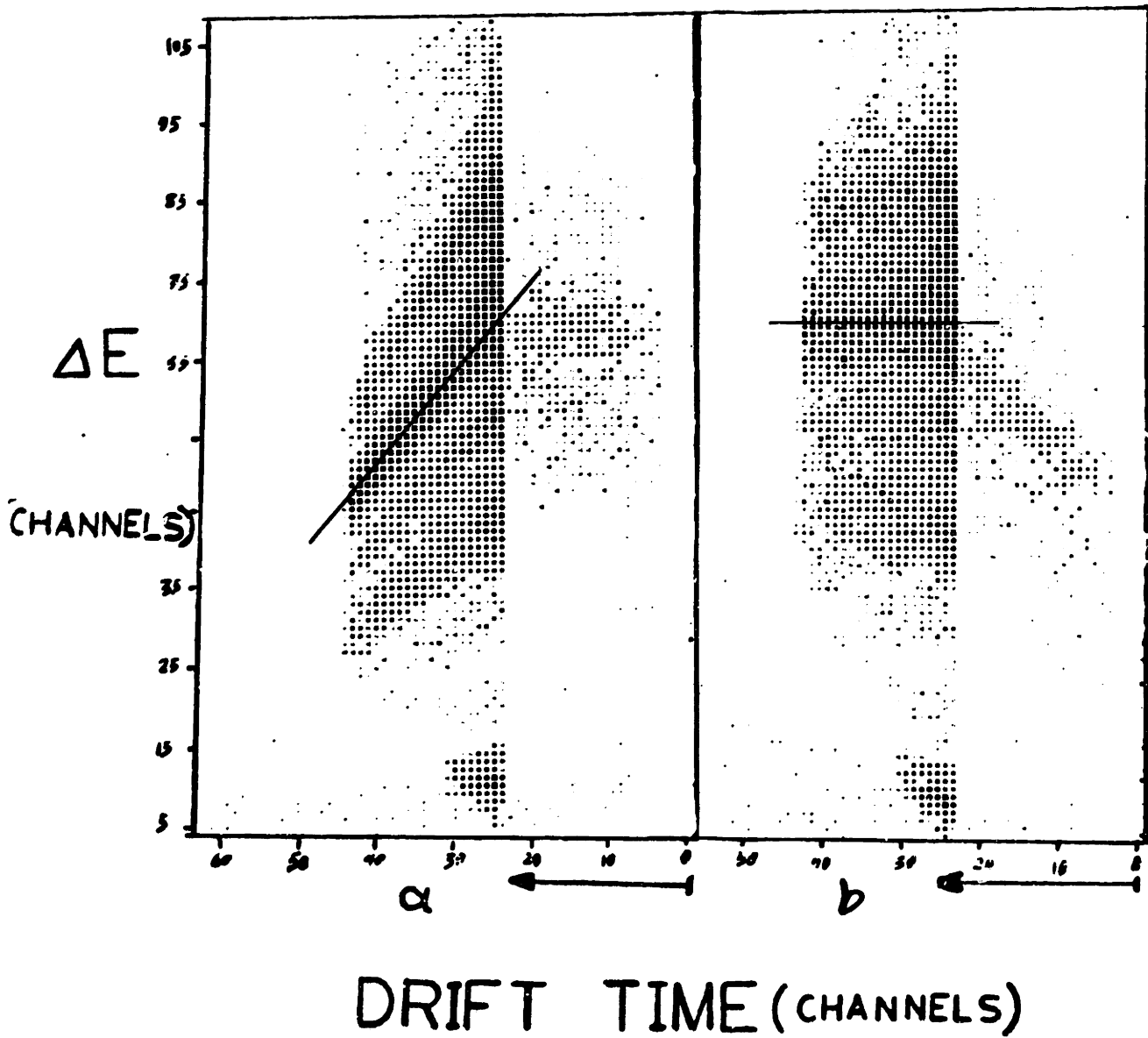


FIGURE 13

linear correction has been made to the ΔE spectra. Figure 13(b) shows the result of such correction for energy loss vs. the drift time.

Calibrations which were made at the end of the experiment in two steps. In the first step, the time information of the time-of-flight, from the TAC, was calibrated. This calibration was done by using pulses from a precision pulse generator which simulates a real signal to the electronic setup of the TOF. Three different delays were applied to the start input of the TAC, 8, 16, and 24 usec, to accomplish this timing calibration. The second step was to obtain energy signals of the SSB alone. This was done by using an oxygen beam of 98 MeV energy on the ^{205}Tl target at $\theta_{\text{lab}} = 70$ degrees. The total energy is the sum of the SSB and the wire signals. A correction has been made to the energy loss in ΔE so that the E signal (like the SSB one) is proportional to the projectile energy. Having the energy loss corrected, one can use the second step of the calibration and the total energy spectrum of the $^{16}\text{O} + ^{205}\text{Tl}$ system to calibrate the energy loss signals, where

$$E_{\text{TOTAL}} = E_{\text{SSB}} + \alpha \Delta E .$$

One should find α such that the elastic peak of the ^{16}O beam in the E_{TOTAL} section agrees with its position in the total energy spectrum (E_T). The total energy itself was later on

calibrated by the use of timing signals to calculate the energy of each particle. For this purpose different isotopes were separated in two steps. In the first step projectile-like particles with the same charge (Z) were separated by use of the $\Delta E-E_T$ technique. Figure 14 shows the energy loss vs. the energy for the ^{16}O induced reactions. Then by sorting the data with gates set on a specific charge region, the nuclei of different masses but same Z are separated. Figure 15 shows two typical $E_T-E_T^2$ spectra for the above reactions. Using the elastic peak and its flight time, one can calibrate the mass spectra for the preceding reactions. From the kinematics of the reaction (as calculated by the code KIN), the energy corresponding to the elastic peak is calculated. The TOF is calibrated by using the calculated energy of the elastic peak and the known flight length (143 cm). These calculated energy and velocity are then used to identify the mass that corresponds to the elastic events on the energy spectrum. The representative channel number for these elastic events is then used as a reference in identifying the masses of the other exit channels. The identified masses and the measured TOF's are used to calibrate the energy spectra of the other channels.

$$E = \frac{1}{2}MV^2$$

The spectral distribution in the excitation energy was computed for each projectile-like particle, from the

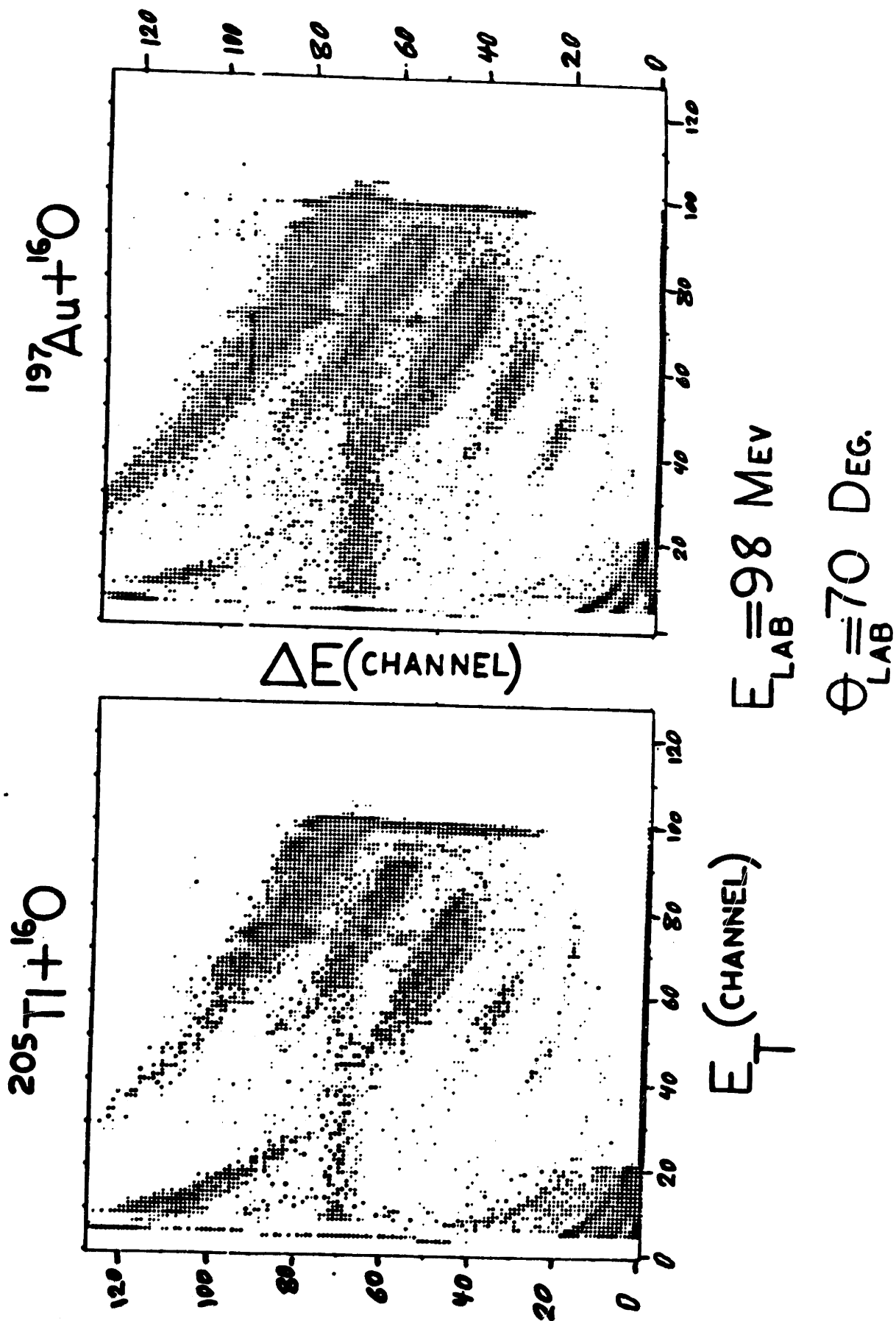
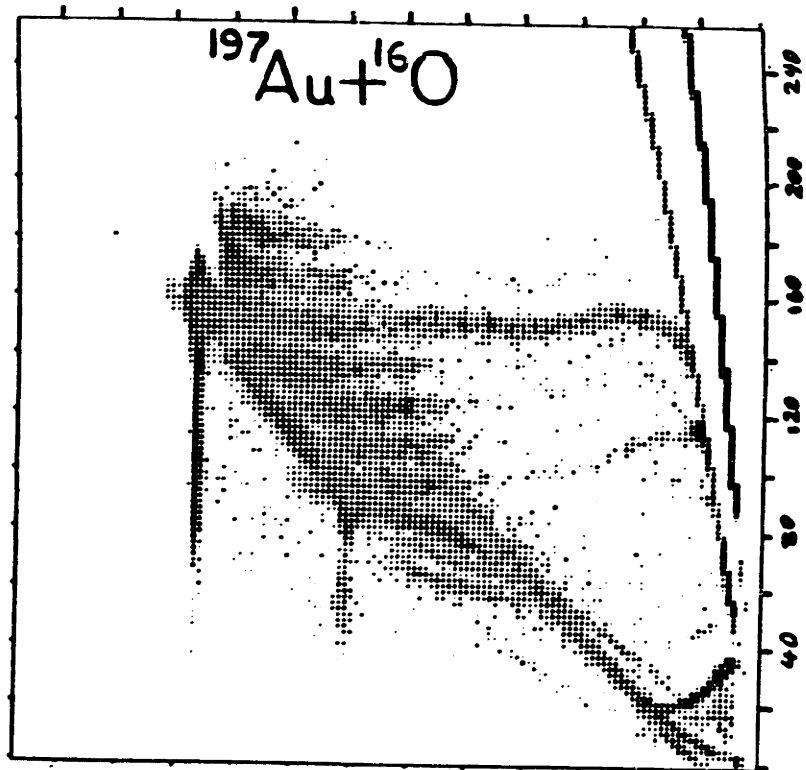


FIGURE 14

$$E_{\text{LAB}} = 98 \text{ MeV} \quad 53$$

$$\theta_{\text{LAB}} = 70^\circ$$



E_T vs $E_T(T-T_0)^2/K$

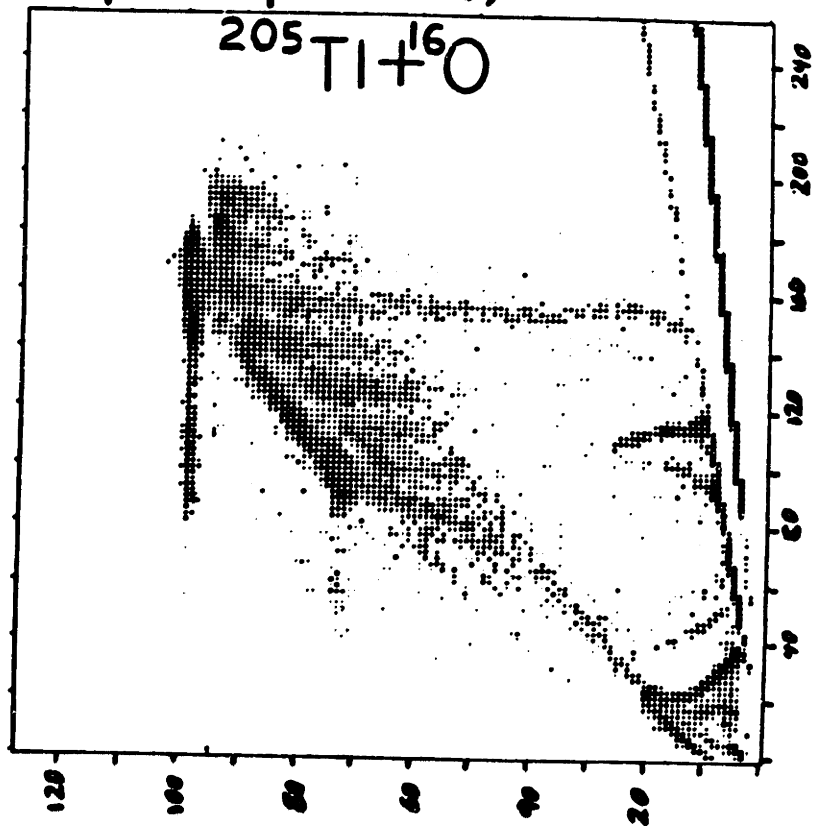


FIGURE 15

kinematic energy spectra, using equations III-3, III-4, and III-8, where the mass for each isotope was taken from the tables of mass. This conversion from kinetic energy to excitation energy has been done such that the energy scales as one Mev per channel. Figures 16 and 17 show the excitation energy spectra for the different exit channels of the grazing reactions for the $^{16}\text{O}+^{205}\text{Tl}$ and the $^{16}\text{O}+^{197}\text{Au}$ systems. As is shown in the figures, for higher excitation energy the spectra tend to drop exponentially indicating that higher excitation states are weakly populated. The optimal excitation energy and spectral shapes are dependent on the number of steps, i.e., the number of nucleons transferred in both directions between the projectile-like nucleus and the target-like one. The available energy at the Coulomb barrier in the exit channel is related to the ground state Q-value Q_0 , and the excitation energy E^* . The optimal effective Q-value $Q_{\text{OPT}}^{\text{EFF}}$ is given by

$$Q_{\text{OPT}}^{\text{EFF}} = Q_0 - E_{\text{OPT}}^* + \Delta V_C,$$

where E_{OPT}^* is the optimal value for the excitation energy and is the peak of the experimental distribution. Tables 1 and 2 include the ground state Q-value, E_{OPT}^* , and the effective optimal Q-value for the different reactions. Figures 18 and 19 show the measured optimal, effective Q-value for the two oxygen induced reactions. Each symbol represents the isotopes of a given charge.

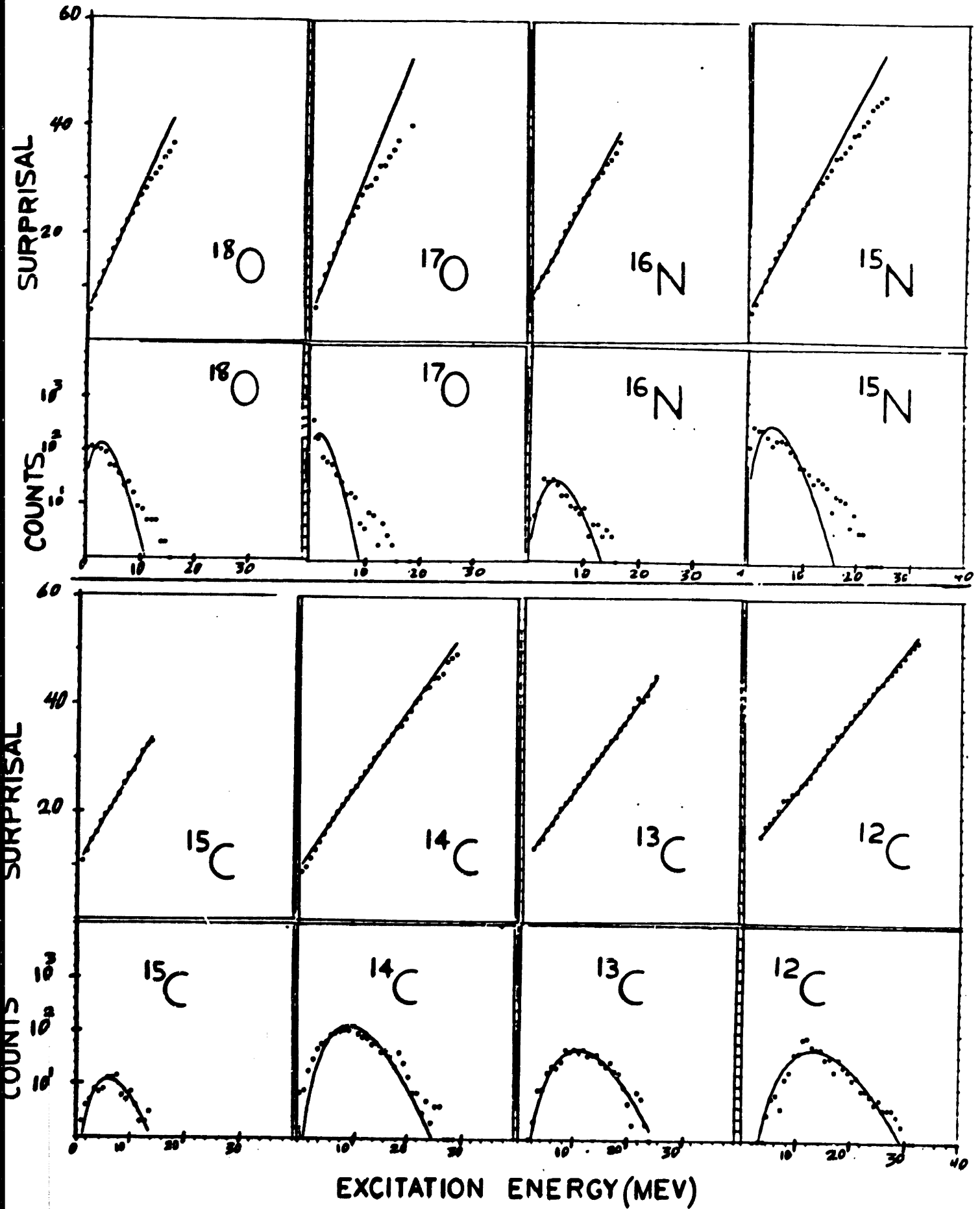


FIGURE 16

$^{197}\text{Au}(160,)^{56}$

$E_{\text{LAB}} = 98 \text{ MeV}$

$\theta_{\text{LAB}} = 70^\circ$

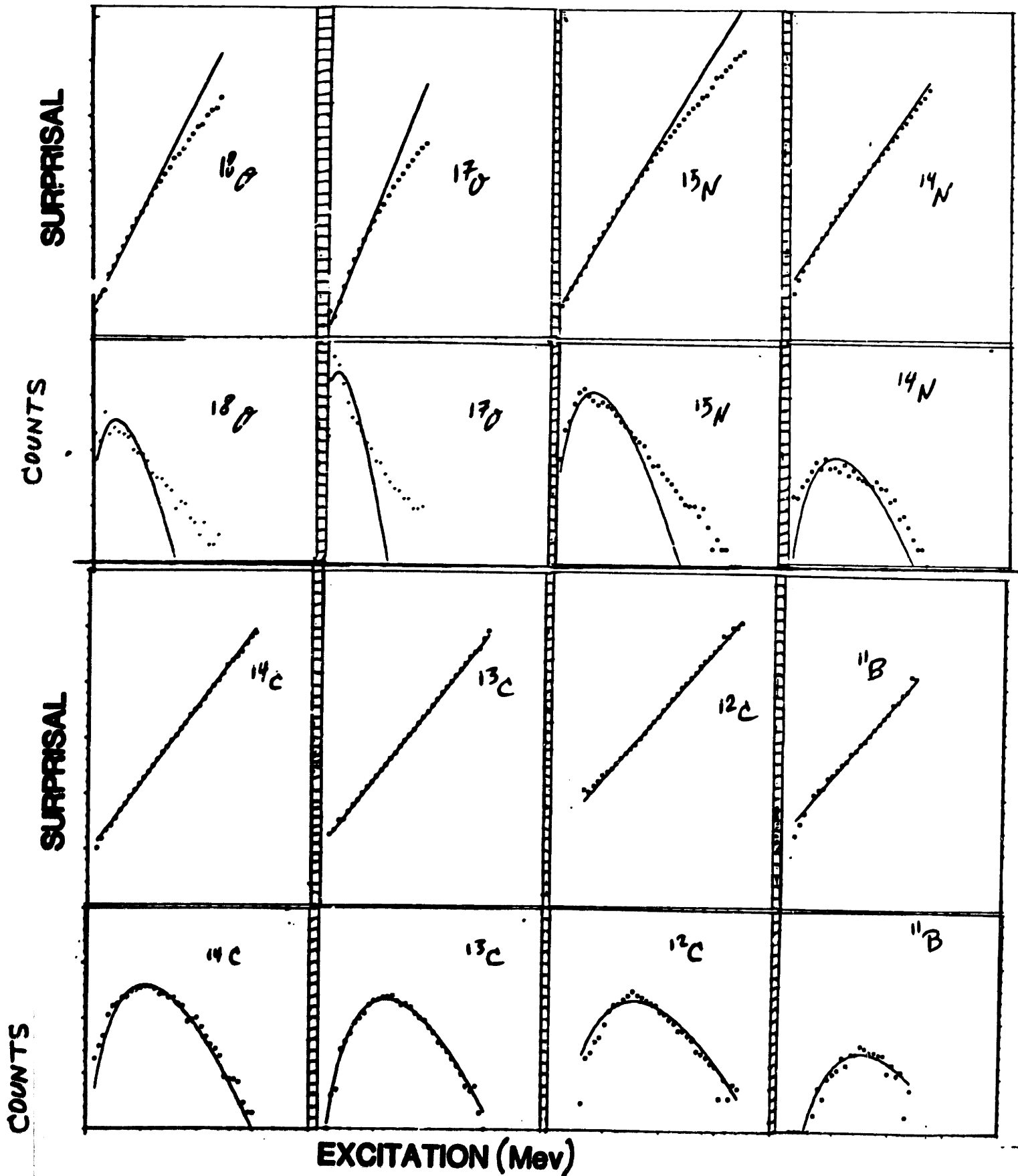


FIGURE 17

$^{205}\text{Tl}(^{16}\text{O}, \text{X})$ $E_{\text{LAB}} = 98 \text{ MeV}$ $\theta = 70^\circ$

SECOND COMPONENT

X	$\Delta S(P/P^{MP})$	$\lambda (\text{MeV})^{-1}$	$\langle E^* \rangle (\text{MeV})$	Q_0	$Q_{\text{OPT}}^{\text{OFF}}$	$E_{\text{OPT}}^* (\text{MeV})$	$Q_{\text{OPT}}^{\text{OFF}}(E_{\text{OPT}}^*) (\text{MeV})$	$\lambda_{12} (\text{MeV})^{-1}$
^{18}O	1.7×10^{-1}	2.28	3.58	-2.07	-5.14	4.88	-6.44	1.3
^{17}O	4.0×10^{-1}	2.99	2.82	-3.40	-5.95	1.10	-4.06	1.4
^{16}N	1.2×10^{-1}	1.88	5.65	-10.5	-8.23	3.30	-5.88	
^{15}N	3.1×10^{-1}	1.95	5.33	-6.20	-3.91	6.77	-5.35	1.4
^{15}C	4.8×10^{-2}	1.76	6.77	-18.3	-9.33			
^{14}C	6.4×10^{-2}	1.46	10.6	-11.5	-6.62	11.0	-7.02	
^{13}C	2.0×10^{-2}	1.39	11.7	-12.8	-9.24			
^{12}C	6.7×10^{-2}	1.28	14.4	-10.3	-9.70	12.0	-7.31	

TABLE I

$^{197}\text{Au}(^{16}\text{O}, X)$

$E_{\text{LAB}} = 98 \text{ MeV}$ $\theta = 70^\circ$

X	$\Delta S(P/P^{\text{mp}})$	$\lambda (\text{Mev})^{-1}$	$K E^*$	$\langle E \rangle (\text{Mev})$	$Q_0 (\text{mev})$	$Q_{\text{OPT}}^{\text{eff}} (\text{mev})$	$E_{\text{OPT}}^* (\text{Mev})$	$Q_{\text{OPT}}^{\text{eff}} (E_{\text{OPT}}^*) (\text{Mev})$	SECOND COMPONENT $\lambda_2 (\text{Mev})^{-1}$
^{18}O	2.5×10^{-1}	1.99	4.68	-2.56	-6.73	6.16	-8.21	1.2	
^{17}O	2.1×10^{-1}	2.57	2.38	-3.94	-6.06	3.71	-3.39	1.4	
^{16}N	1.2×10^{-2}	1.73	6.55	-10.8	-9.67	3.69	-7.95		
^{15}N	9.3×10^{-2}	1.66	7.29	-5.02	-4.85	8.98	-6.54	1.25	
^{14}N	1.3×10^{-1}	1.48	9.52	-9.21	-11.5	11.4	-13.4		
^{15}C	3.1×10^{-1}	1.56	8.74	-18.3	-11.6				
^{14}C	1.7×10^{-2}	1.35	11.9	-10.8	-7.50	13.7	-9.25		
^{13}C	5.0×10^{-3}	1.29	13.3	-12.0	-10.3	15.0	-12.0		
^{12}C	3.5×10^{-2}	1.16	16.8	-8.65	-10.8	18.7	-12.7		
^{11}B	4.7×10^{-2}	1.20	15.6	-19.8	-12.6	17.5	-14.5		

TABLE 2

The optimal energy loss as a function of nucleon transfer for the reactions (figures 18 and 19) has the same general behavior as the data reported by Mikumo et al [10] (shown in figure 20). However, we see that the dependence of Q_{OPT}^{EFF} with ΔN here is clearly not linear, as in [4]. A non-linear dependence of Q_{OPT}^{EFF} with ΔN was also observed for the $^{16}O + ^{232}Th$ system [3]. From a close look at figures 18 and 19 for both reactions and also the results of the reactions like $^{16}O + ^{232}Th$ [3], it is clear that there is a noticeable increase in the Q_{OPT}^{EFF} for ^{15}N in the $^{16}O + ^{205}Tl$ reaction, in which the heavy ejectile would be $^{206}_{82}Pb$. This effect also appeared in figures 21 and 22. In these figures energy-integrated yields, which are proportional to the branching ratio for each exit channel, are plotted vs. the number of steps ΔN . These yields seem to have an exponential dependence on ΔN .

In Karp et al. [3] it was found that the branching ratio $P(n)$ had a dependence on the number of steps ΔN given by

$$P(n) = \exp[-(\Delta N + 2l)],$$

where l is an integer describing which "line" a particular exit channel (projectile like particle) belongs to. Each line corresponds to a different number of proton pickups.

In a more clear way of illustrating this change on ^{15}N of the reaction $^{16}O + ^{205}Tl$, we can compare the yield for ^{15}N to

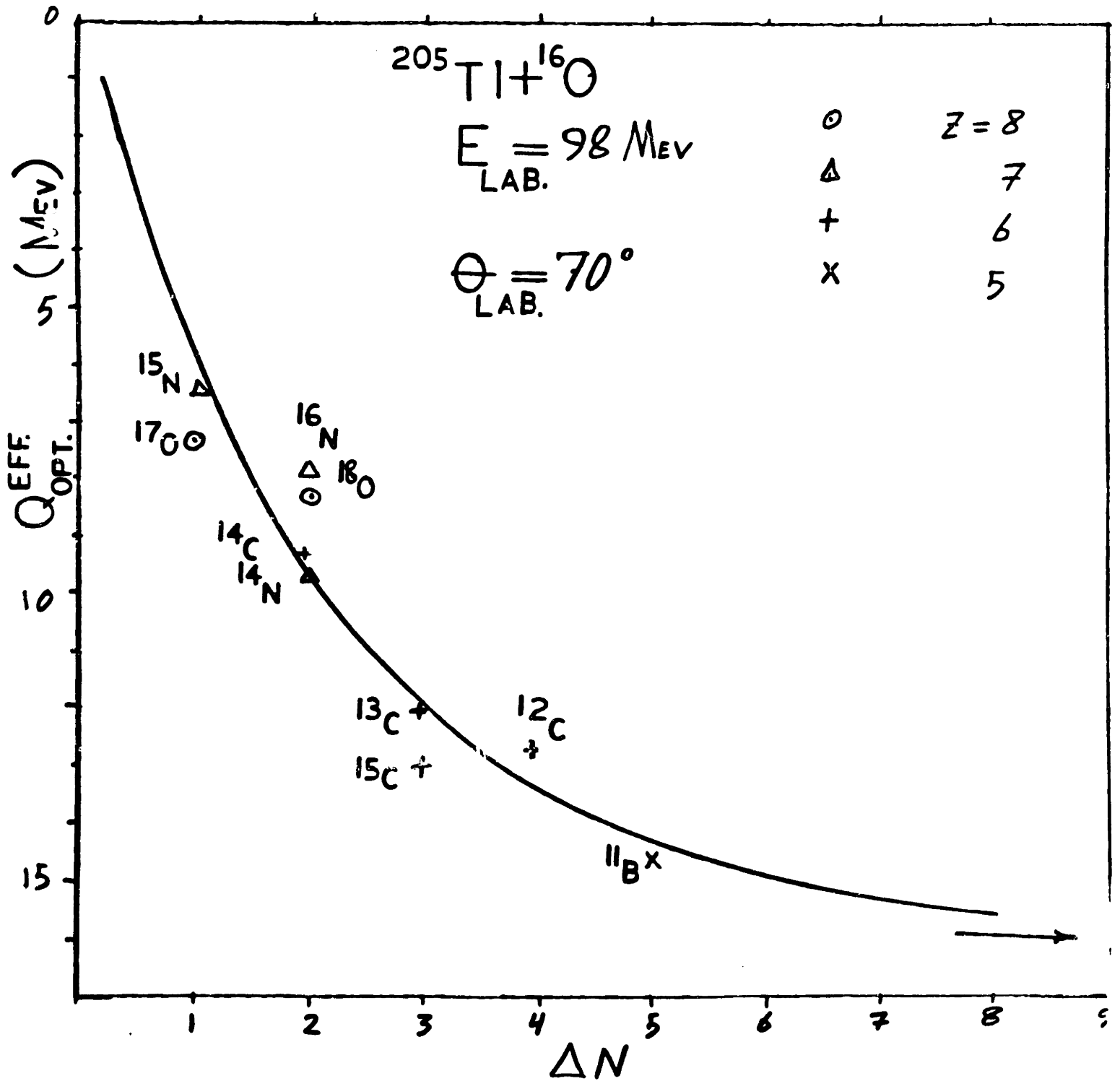


FIGURE 18

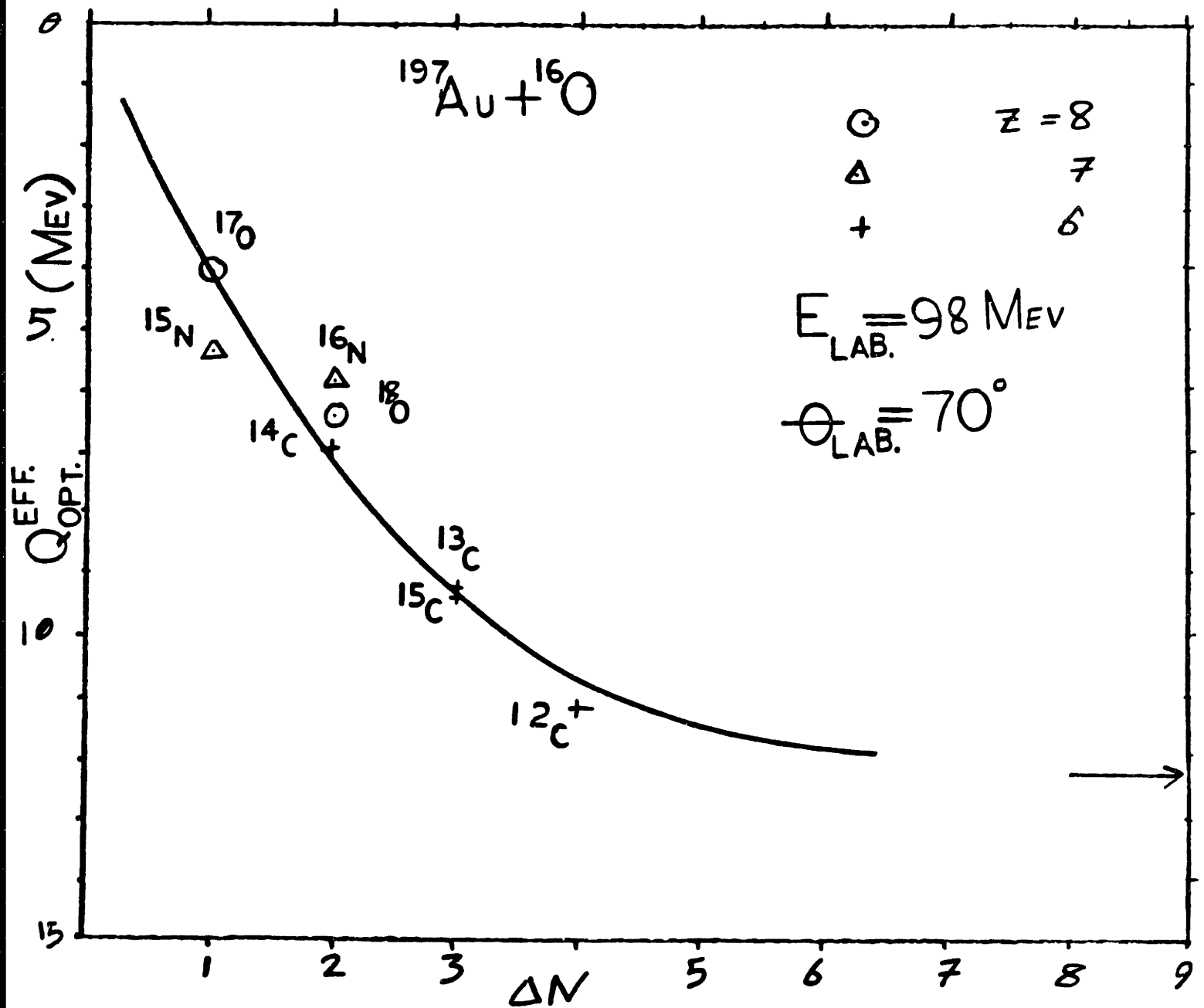


FIGURE 19

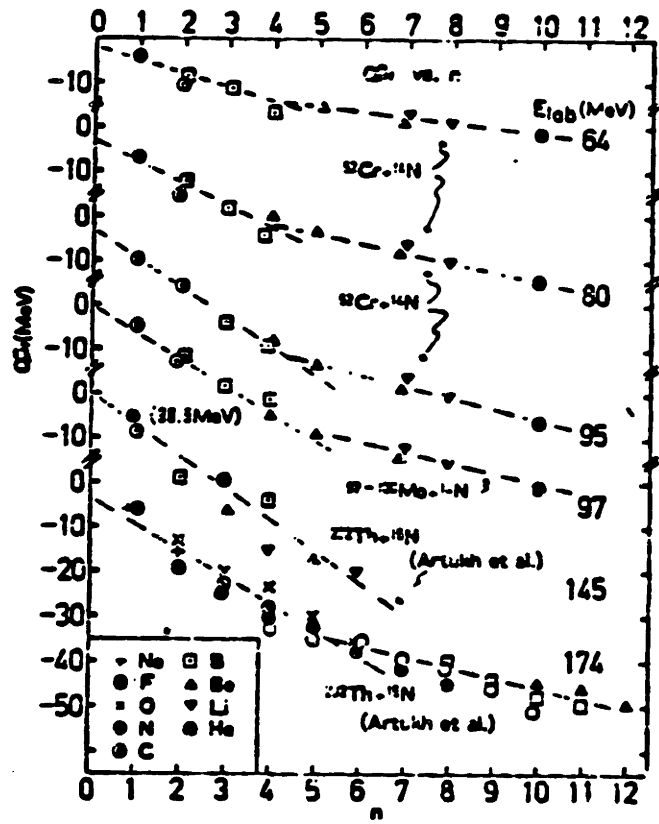


Figure 20

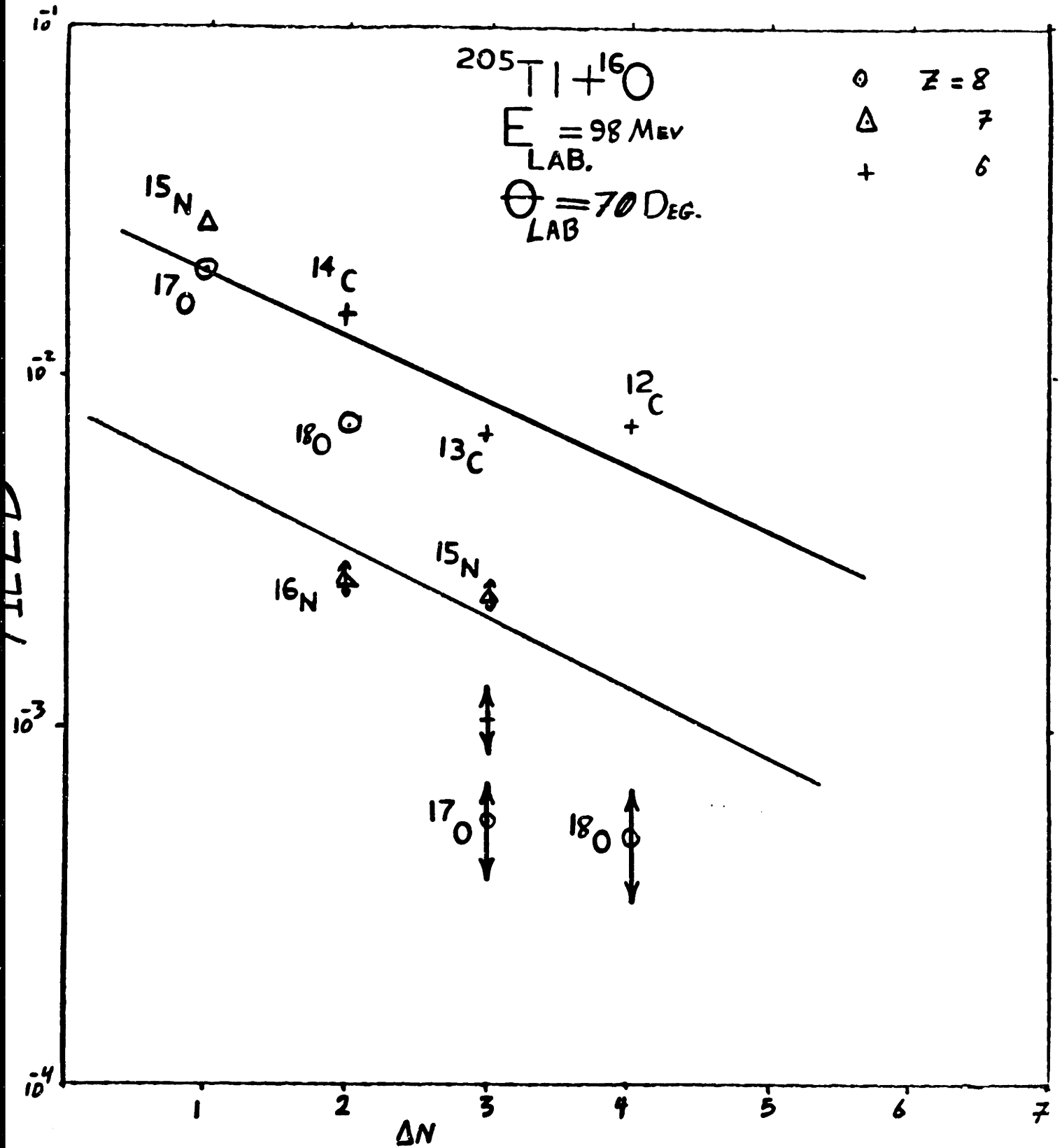


FIGURE 21

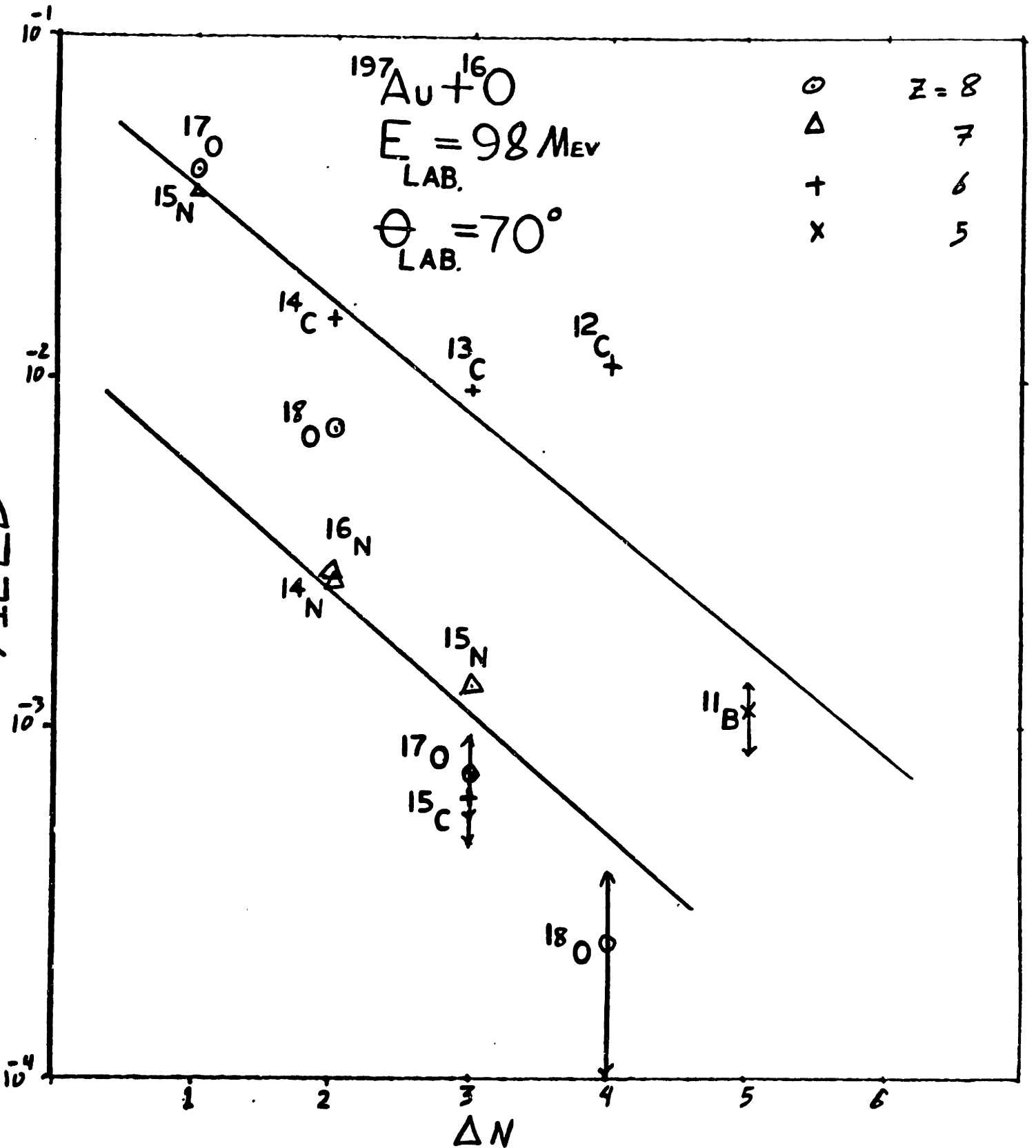


FIGURE 22

another exit channel like ^{17}O for both reactions of ^{16}O on ^{197}Au and ^{205}Tl . We see that the position of these two exit channels are completely changed relative to each other, or yield ^{15}N for one nucleon transferred divided by yield ^{17}O for one nucleon transferred for ^{205}Tl is about 1.29 whereas for the gold target it is 0.87. In other words, the position of ^{15}N relative to that of ^{17}O in other reactions like $^{16}\text{O} + ^{232}\text{Th}$ [3] and $^{16}\text{O} + ^{197}\text{Au}$ are little bit lower than ^{17}O , whereas for reaction $^{16}\text{O} + ^{205}\text{Tl}$ it is now at a higher cross-section than the cross section for the ^{17}O exit channel. A question might come about ^{16}N , why ^{16}N is not acting the same as ^{15}N in the $^{16}\text{O} + ^{205}\text{Tl}$ reaction but, we should realize that the channel of ^{15}N (one nucleon transfer) is a very simple case of a transfer reaction. On the contrary, the system $^{16}\text{O} + ^{205}\text{Tl}$ with the exit channel of ^{16}N (bi-directional two nucleon transfer) is a rather complicated case for the above model for $Q_{\text{OPT}}^{\text{EFF}}$.

One might think that this effect on the effective optimal Q -value is due to the ground state Q -value calculation by using the table of masses. If we were to use liquid droplet mass formula (LDMF) we can avoid the effect of the extra stability of the ground state configuration, which would not affect the nucleus at higher excitation. But the calculation of the Q_0 by using this technique did not recover the change in $Q_{\text{OPT}}^{\text{EFF}}$ for the ^{15}N channel in the $^{16}\text{O} + ^{205}\text{Tl}$ reaction. It changes the relative position of the ^{15}N to the ^{17}O channel, and makes the value of $Q_{\text{OPT}}^{\text{EFF}}$ for ^{15}N to be very much smaller

than ^{17}O . I.e., the ground state Q-value was -6.2 MeV where by using the LDMF it becomes $+4.5$ MeV. So, this simple model is no longer applicable.

A surprisal analysis has been made on the excitation energy spectra for all projectile-like particles in the exit channels. The surprisal function for each channel is shown in figures 16 and 17. From the average excitation energy or the centroid $\langle E^* \rangle$ of the distributions, the lagrangian parameters (λ_0, λ_1) are calculated. For this calculation the following relationship has been used

$$P^{\text{ME}}(E^*) = P_0(E^*) \exp(-\lambda_0 - \lambda_1 E^*)$$

where

$$\sum_i P^{\text{ME}}(E^*) E^* = \langle E^* \rangle,$$

together with the normalization condition

$$\sum_i P^{\text{ME}}(E^*) = 1.$$

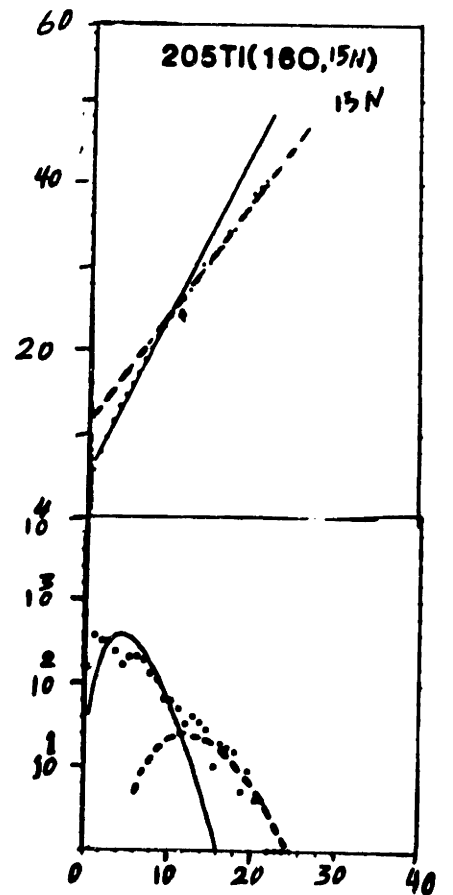
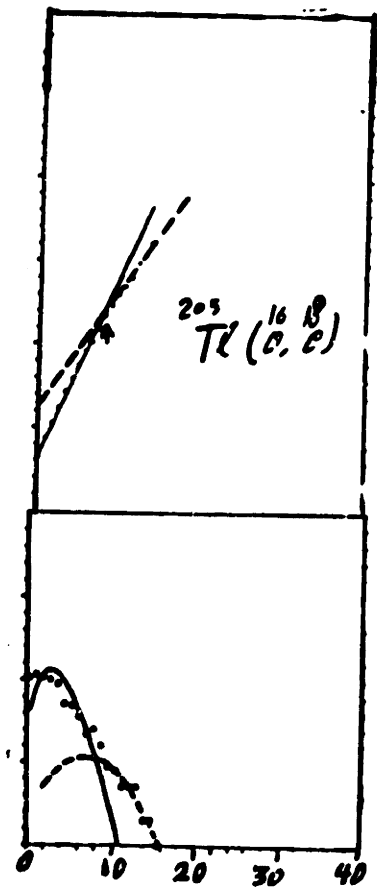
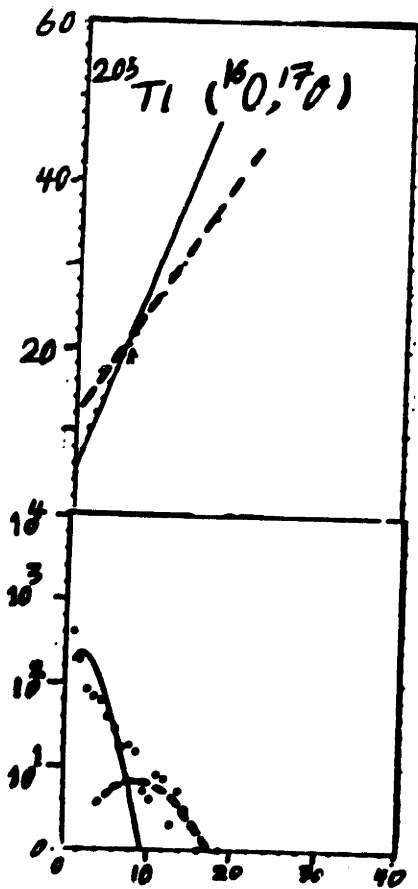
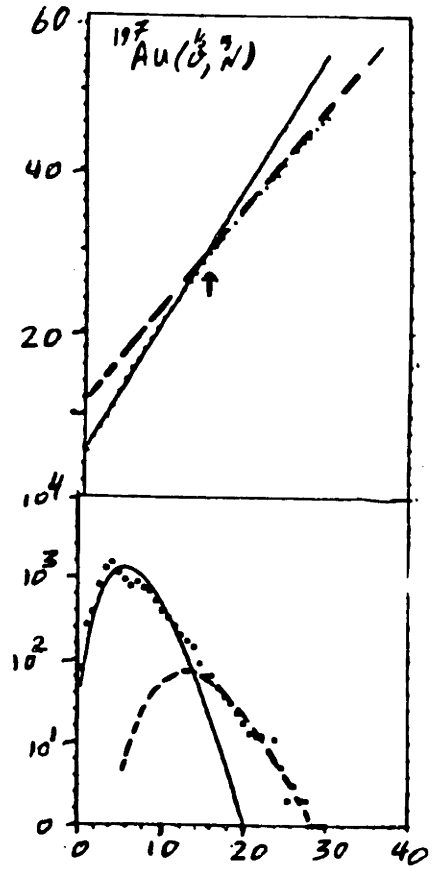
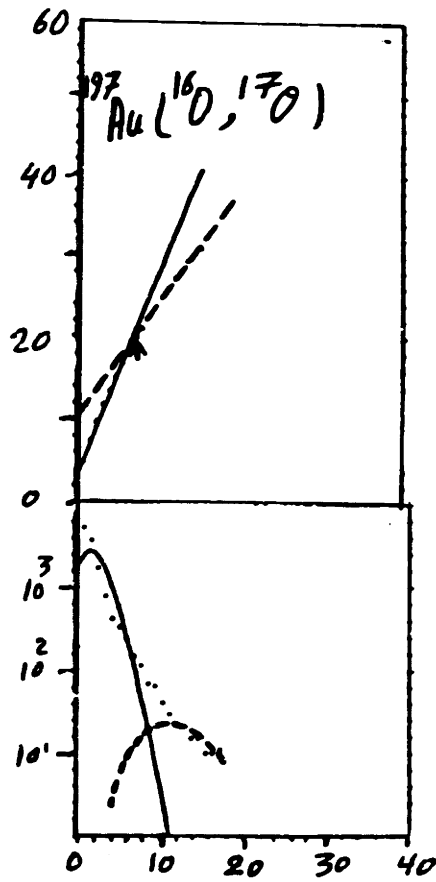
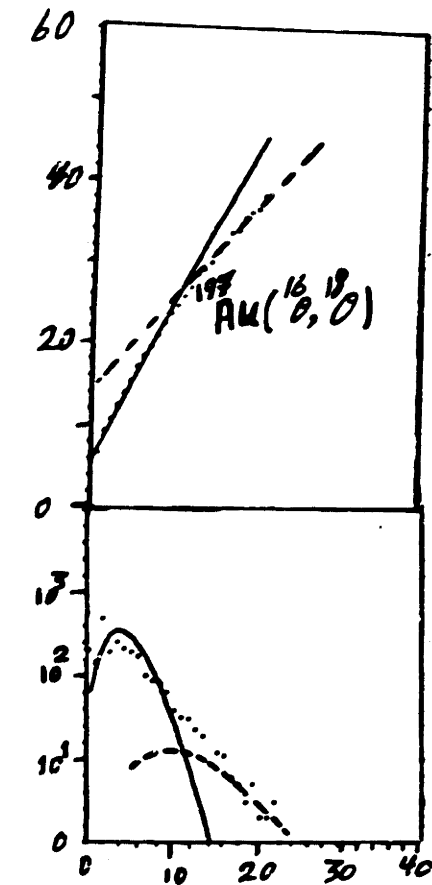
A computer program has been used to find λ_0 and λ_1 for each excitation energy spectrum (ENTRPY1). For the input of this program another program, PROG1, has been used to calculate the prior distribution. As described in chapter II, the Fermi gas level density has been used with the excitation energy corrected for rotational and pairing energies, where

$$E_{ROT} = \frac{l(l+1)\hbar^2}{2I_{RMC10}}$$

$$E = 12 \delta A^{-1/2}$$

where $\delta=0$ for odd-odd, $\delta=1$ for odd-even, $\delta=2$ for even-even. In the above calculation for ^{16}O on ^{197}Au and ^{205}Tl the pairing energy correction has been relatively small compared to the average excitation energy.

Tables 1 and 2 show the values of the average excitation energies and of the parameters λ , the entropy deficiency or information contents ($S = -\sum_i P_i \ln(P_i / P_i^0)$). The most probable distributions with one constraint are indicated by solid curves on figure 23. The figure shows a large systematic deviation in the surprisal plots of the ^{17}O , ^{18}O , and ^{15}N for the reactions $^{16}\text{O} + ^{197}\text{Au}$ and $^{16}\text{O} + ^{205}\text{Tl}$ in the region of high excitation energy, indicated by the arrows. So, a second alternative for the above reactions is considered, where each of the reactions are considered to have two components. Each of these components has a different number of steps taken for the reaction. For example, for the case of the ^{15}N (figure 23), the slope of the high excitation part of the spectrum is nearly the same as the 3-nucleon transfer to ^{13}C . This suggests [3] that there are two components to the energy spectrum. These are a 1-nucleon transfer part, peaked at low excitation energy, and a 3-nucleon transfer part, peaked at a high excitation energy, in which 2-nucleons transfer from the projectile to the target and 1-nucleon transfers in the



EXCITATION ENERGY (Mev)

reverse direction. The fraction of the cross-section of the second component (figure 23) of the total is about 8%. Likewise, for the ^{18}O channel, we have a 2-nucleon transfer component and a 4-nucleon transfer component. The fraction of the cross-section for the second component is 5% of the total. These values of cross-section contribution to the total cross-section are given in table 3. Figure 23 shows the second component for ^{17}O , ^{18}O , ^{15}N exit channels for above reactions.

By this method we may explain almost all of the reaction channels from ^{16}O on ^{205}Tl and ^{197}Au , with $E_{\text{lab}}=98$ MeV and $\theta_{\text{lab}}=70$ degrees in terms of only one constraint distributions. Therefore, the shapes of the distributions of these reactions depend only on the average energy about which the distributions are peaked and the number of the transferred nucleons.

$$E_{\text{LAB.}} = 98 \text{ MeV.}$$

$$\theta_{\text{LAB.}} = 70^\circ$$

$$^{205}\text{TI}(^{16}\text{O}, X)$$

TABLE-3

X	YIELD				
	TOTAL	FIRST COMPONENT	SECOND COMPONENT	FIRST COMP. %	SECOND COMP. %
^{18}O	$.769 \times 10^{-2}$	$.730 \times 10^{-2}$	$.387 \times 10^{-3}$	95.1	4.90
^{17}O	2.11×10^{-2}	2.06×10^{-2}	$.552 \times 10^{-3}$	97.4	2.60
^{16}N	$.254 \times 10^{-2}$				
^{15}N	2.88×10^{-2}	2.65×10^{-2}	$.231 \times 10^{-2}$	92.1	7.90
^{15}C	$.106 \times 10^{-2}$				
^{14}C	1.50×10^{-2}				
^{13}C	$.698 \times 10^{-2}$				
^{12}C	$.728 \times 10^{-2}$				

$$^{197}\text{Au}(^{16}\text{O}, X)$$

X	YIELD				
	TOTAL	FIRST COMPONENT	SECOND COMPONENT	FIRST COMP. %	SECOND COMP. %
^{18}O	$.732 \times 10^{-2}$	$.710 \times 10^{-2}$	$.221 \times 10^{-3}$	96.8	3.20
^{17}O	4.02×10^{-2}	3.95×10^{-2}	$.740 \times 10^{-3}$	98.2	1.80
^{16}N	2.61×10^{-3}				
^{15}N	3.59×10^{-2}	3.46×10^{-2}	1.34×10^{-3}	96.3	3.70
^{15}C	$.640 \times 10^{-3}$				
^{14}C	1.53×10^{-3}				
^{13}C	9.42×10^{-3}				
^{12}C	1.02×10^{-2}				
^{11}B	1.14×10^{-3}				

V- SUMMARY AND CONCLUSIONS

Energy spectra from different projectile-like particles have been measured and excitation energy spectra corresponding to each target-like fragment have been calculated. Then, surprisal analysis has been applied on the reactions $^{16}\text{O} + ^{205}\text{Tl}$ and $^{16}\text{O} + ^{197}\text{Au}$ at beam energy of 98 MeV and near the grazing angle of 70 degrees.

A surprisal analysis with one constraint showed that for certain exit channels one sees the contributions of the different processes to the cross-section. For example, in the reaction $^{197}\text{Au}(^{16}\text{O}, ^{15}\text{N})$, it is probable to have a transfer of 1- and 3-nucleons. Also, for the exit channel of ^{18}O , there are two or more possible processes for which the most probable one is 2-nucleon transfer, followed by 4-nucleon transfer. The behavior was also seen by Karp et al. [3] in the ^{17}O and ^{15}N exit channels, for the $^{232}\text{Th}(^{16}\text{O}, \text{X})$ reaction. Almost all of the energy spectra can be explained in terms of distributions of maximal entropy subject to one constraint.

Also, effective optimal Q -value $Q_{\text{OPT}}^{\text{OFF}}$ and energy-integrated yields were obtained versus the number of nucleons transferred. A noticeable behavior in $Q_{\text{OPT}}^{\text{OFF}}$ and energy-integrated yields for the ^{15}N exit channel of the

$^{16}\text{O} + ^{205}\text{Tl}$ reactions has been observed which could be due to the $Z=82$ closed shell structure of the heavy ejectile ^{205}Pb in this reaction. This behavior was not observed for ^{16}N channel, which might be due to the complex 2-nucleon bi-directional transfer compared to the 1-nucleon transfer of the ^{15}N channel.

The validity of the above conclusions is confined to the data obtained from the two oxygen induced reactions. It would be useful to extend the measurements with the gold target, so that data with good enough statistics in the multi-nucleon transfer might be collected. This may allow the observance of the $Z=5,6$ projectile-like isotopes. These distributions, in turn, may also show shell effects. Likewise, extension of the measurements, with the ^{205}Tl target, could result in observation of other nitrogen channels. Such a measurement could lead to a definite conclusion about the observations reported in the present work.